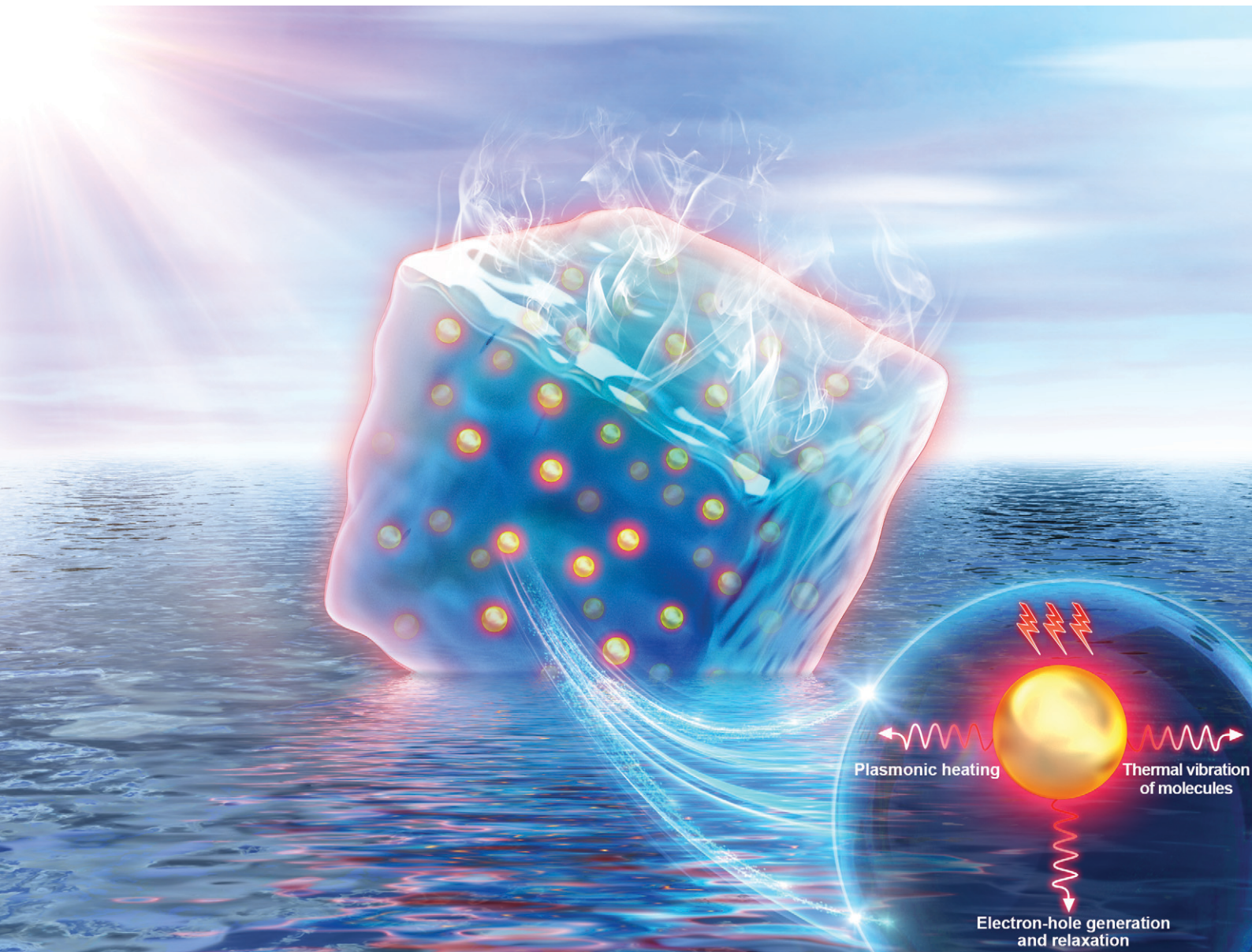


Environmental Science Nano

rsc.li/es-nano



ISSN 2051-8153

CRITICAL REVIEW

[View Article Online](#)
[View Journal](#) | [View Issue](#)



Cite this: *Environ. Sci.: Nano*, 2022,
9, 2264

Advances and challenges of broadband solar absorbers for efficient solar steam generation

Ying Liu,^{†c} Jian Zhao, ^{ID}^{†cd} Siyu Zhang,^{†b} Dengyu Li,^b Xuejiao Zhang, ^{ID}^{*b} Qing Zhao ^{ID}^{*ab} and Baoshan Xing ^{ID}^e

With the emergence of a large number of solar absorbers due to the tremendous development of material science, an ancient technology, solar-driven evaporation offers a promising opportunity for addressing the global water crisis in a green, feasible, efficient, economic, and sustainable way. To achieve high evaporation performance, solar absorbers with broad solar absorption and high photothermal conversion efficiency are anticipated. In this review, we summarized the recent progress on solar absorbers, including metallic nanoparticles, carbonaceous materials, conjugated polymers, organic-small-molecule solar absorbers, and semiconductors. On account of understanding the working mechanisms, the strategies to rational design, property modulation, and structural optimization of solar absorbers for improving the performance of solar-driven evaporation are discussed. Meanwhile, the heat management and water transportation in the state-of-the-art evaporation systems are also highlighted with representative examples. Finally, we overview the key challenges that restrict the translation from laboratory to practical solar-driven evaporation for clean water production.

Received 24th January 2022,
Accepted 18th April 2022

DOI: 10.1039/d2en00070a

rsc.li/es-nano

Environmental significance

Water crisis is one of the major threats for the sustainable development of global society. Solar-driven evaporation has drawn extensive attention as an environmentally benign and sustainable technique for freshwater generation, since it can separate freshwater from salt, mineral, and other impurities, by using the abundant and renewable sunlight as the only driving force, thus leading to CO₂ emission reduction and minimum environmental impact. To advance the progress of solar-driven evaporation, it is rational either to utilize the already-existing photothermal materials and engineer them to enhance the photothermal performance, or to develop novel solar absorbing materials with more remarkable properties. This review provides a preliminary guidance for solar absorber design, selection, and optimization, as well as evaporation system engineering for efficient solar-driven evaporation in practice.

1. Introduction

Water crisis is one of the major threats for the sustainable development of global society, which has been further exacerbated in recent years, with the explosive growth of

world population, contamination of freshwater resources, and climate change.¹ Although water, as one of the most abundant resources on Earth, covers three-fourths of the

^aNational-Regional Joint Engineering Research Center for Soil Pollution Control and Remediation in South China, Guangdong Key Laboratory of Integrated Agro-environmental Pollution Control and Management, Institute of Eco-environmental and Soil Sciences, Guangdong Academy of Sciences, Guangzhou 510650, China

^bKey Laboratory of Pollution Ecology and Environmental Engineering, Institute of Applied Ecology, Chinese Academy of Sciences, Shenyang 110016, China.

E-mail: zhangxuejiao@iae.ac.cn, zhaoqing@iae.ac.cn

^cInstitute of Coastal Environmental Pollution Control, Ministry of Education Key Laboratory of Marine Environment and Ecology, Ocean University of China, Qingdao 266100, China

^dLaboratory for Marine Ecology and Environmental Science, Qingdao National Laboratory for Marine Science and Technology, Qingdao 266071, China

^eStockbridge School of Agriculture, University of Massachusetts, Amherst, MA 01003, USA

† These authors contributed equally to this work.



Ying Liu

Ying Liu is currently studying for a master's degree at Ocean University of China and co-trains at Institute of Applied Ecology, Chinese Academy of Sciences. Her current research interests mainly focus on solar water desalination and photocatalytic degradation of environmental pollutants.

Earth's surface, ~97% of water resources are generally brackish water that requires desalination before effective utilization.^{2,3} To date, various technologies, including reverse osmosis,^{4,5} electrodialysis,⁶ and membrane distillation,⁷ have been developed for purifying saline water into freshwater. However, these traditional desalination technologies need the driving force deriving from electrical energy, thermal energy, and mechanical energy, which not only is energy- and cost-intensive, but also always induces the emission of greenhouse gases and even severe environmental problems.⁸ Therefore, the development of alternative technologies that are energy-efficient and low-cost is urgently needed to conquer the global challenge of freshwater scarcity.

Solar-driven evaporation is the critical stage in the natural hydrological cycle, which allows the replenishment of land freshwater.⁹ Inspired by the natural evaporation process,

solar-driven evaporation has drawn extensive attention as an environmentally benign and sustainable technique for freshwater generation, since it can separate freshwater from salt, mineral, and other impurities, by using the abundant and renewable sunlight as the only driving force, thus leading to CO₂ emission reduction and minimum environmental impact.¹⁰ A systematic literature search was conducted in the Web of Science database (<https://www.isiknowledge.com>). By using “solar evaporation”, “photothermal conversion”, or “solar distillation” as keywords, we retrieved articles from 2011 to 2021. After preliminary and secondary screening, phrases that are not relevant, such as “solar cells” and “photothermal treatment of cancer”, were filtered out. VOSviewer was used to build a social network map, where the size of the node and the thickness of the line indicated the importance of keywords,



Jian Zhao

Jian Zhao is currently a full professor in Ocean University of China. He received his PhD degree from Ocean University of China in 2011 under the supervision of Prof. Zhenyu Wang. As a Postdoctoral Fellow, he joined Prof. Baoshan Xing's group at the University of Massachusetts Amherst in 2012. In 2014, he came back to Ocean University of China. His current research interests focus on the environmental geochemical processes of engineered nanoparticles, environmental applications of nanomaterials in contamination removal and disinfection, and environmental behaviors of microplastics.



Xuejiao Zhang

and clean energy applications, including organic/inorganic hybrid nanomaterials for solar desalination, water disinfection, and resource recovery.



Siyu Zhang

focus on designing functional two-dimensional nanomaterials in environmental and health fields by employing quantum chemical calculations.



Qing Zhao

Qing Zhao received his PhD degree from the Institute of Applied Ecology, Chinese Academy of Sciences in 2010. During 2010–2014, he worked with Prof. Baoshan Xing as a post doctor. Afterwards, he joined the Institute of Applied Ecology, Chinese Academy of Sciences and worked as a professor. His research interests focus on safety assessment of nanomaterials and their potential applications in the environmental field.

and the color of the nodes represented the occurrence time of keywords (Fig. 1). Obviously, the occurrence frequencies of “evaporation efficiency”, “photothermal conversion materials”, “desalination”, “solar steam generation”, and “photothermal conversion efficiency” have been growing in the last two years, indicating that more and more attention has been paid to the performance and efficiency of solar absorbers. Considering that solar absorbers allow direct energy transformation from solar power into thermal energy, to advance the progress of solar-driven evaporation, it is rational either to utilize the already-existing solar absorbers and engineer them to enhance the photothermal performance, or to develop novel solar absorbing materials with more remarkable properties.

Thanks to the advanced achievements in materials science, a large number of solar absorbers with capacities of sunlight harvesting and photothermal conversion have been rapidly developed, which endow the solar-driven evaporation technology with improved efficiency and enable the old concept to regain attention as a green technique for clean water generation.¹¹ Researchers have explored the potential application of a variety of solar absorbers, including metallic nanoparticles, carbonaceous materials, semiconductors, and polymers, in solar-driven evaporation.^{11,12} Among them, metallic nanoparticles and black carbon were applied in the early stages, while some carbonaceous materials (*e.g.*, graphene oxide, carbon nanotubes and polymers) and newly-developed materials (*e.g.*, metal organic frameworks and graphitic carbon nitride) have been new research hotspots in recent years (Fig. 2). The light harvesting capacity of solar absorbers can be enhanced in terms of both intensity and width of sunlight absorption by a variety of strategies, such as modulation of materials' composition, size, morphology, surface coating and band gap, and hybridization of diverse solar absorbers.^{13,14} Apart from the excellent optical properties, the chemical stability, toxicity, scalability, and economic cost are also important parameters for the selection of solar absorbers. Although some reviews have mentioned the importance of solar absorbers in the performance of solar evaporators, it is still necessary to comprehensively discuss the properties, pros and cons, and more importantly the solar-to-thermal conversion mechanisms of each type of solar absorber. On this basis, it is feasible to select the optimal solar absorber as needed and maximize its solar absorptance by the suitable strategy.

In this review, we first summarize the fundamental knowledge and general concept of photothermal conversion regarding the development of effective solar absorbers. Then we briefly introduce the development of four types of solar-driven evaporation systems, from bottom and volumetric heating to interfacial and isolation heating. The latter two patterns minimize the heat losses and optimize the solar energy utilization by localized heating. Based on the different interaction mechanisms between electromagnetic radiation and materials, the solar absorbers are categorized into plasmonic heating, thermal vibration of molecules, and electron-hole generation and relaxation. On the basis of

understanding the photothermal conversion mechanisms, this review emphasizes on the rational design and sophisticated optimization strategies for improved solar absorption and photothermal conversion, and elaborates on how these advanced solar absorbers, together with optimal thermal management and water transportation by structural engineering, synergistically improve the performance of solar-driven evaporation. Finally, the current achievements, remaining challenges, and promising future directions, from the perspective of both academic research and practical use, are addressed. This review provides a comprehensive understanding of photothermal conversion and a preliminary guidance for solar absorber design, selection, and optimization, as well as evaporation system engineering for efficient solar-driven evaporation.

2. General concept of solar evaporation systems

2.1 Critical factors for efficient solar absorbers

A solar absorber (or photothermal material) is one of the core components of solar evaporation systems that determine the evaporation efficiency. When the solar absorbers receive electromagnetic radiation (sunlight), an electric field induced by light drives the mobile carriers in the materials, facilitating the conversion of gained energy in the carriers into thermal energy *via* photoexcitation.^{11,15} An ideal solar absorber should fulfill the following criteria: i) broadband and highly efficient optical absorption with minimal transmittance and reflectance across the entire solar spectrum (300–2500 nm);^{16,17} ii) efficient photo-to-thermal conversion with low thermal emission; iii) low-cost, ease of scale-up, stable, biocompatible, and recyclable.

We will introduce beforehand some formulas commonly used for efficiency calculation in solar-driven evaporation. Solar absorbance (α), representing the material's light absorbing ability, is defined as the ratio of absorbed radiation to the incident solar radiation, which can be calculated using the following formula:

$$\alpha = \frac{\int_{0.3}^{2.5} I_{\text{sol}}(\lambda)(1-R(\lambda))d\lambda}{\int_{0.3}^{2.5} I_{\text{sol}}(\lambda)d\lambda} \quad (1)$$

where I_{sol} is the normal solar spectral irradiance defined by ISO standard 9845-1 (1992) at air mass (AM) 1.5, and $R(\lambda)$ is the total reflectance at a certain wavelength.¹⁸

In addition to water vaporization, the heat generated by solar absorbers can be consumed mainly *via* three ways (conduction, convection, and radiation) (Fig. 3).^{19,20} Heat conduction (Q_{cond}) induces the heat loss to bulk water due to the temperature gradient between the solar absorber and bulk water.

$$Q_{\text{cond}} = Cm(T_1 - T_2) \quad (2)$$

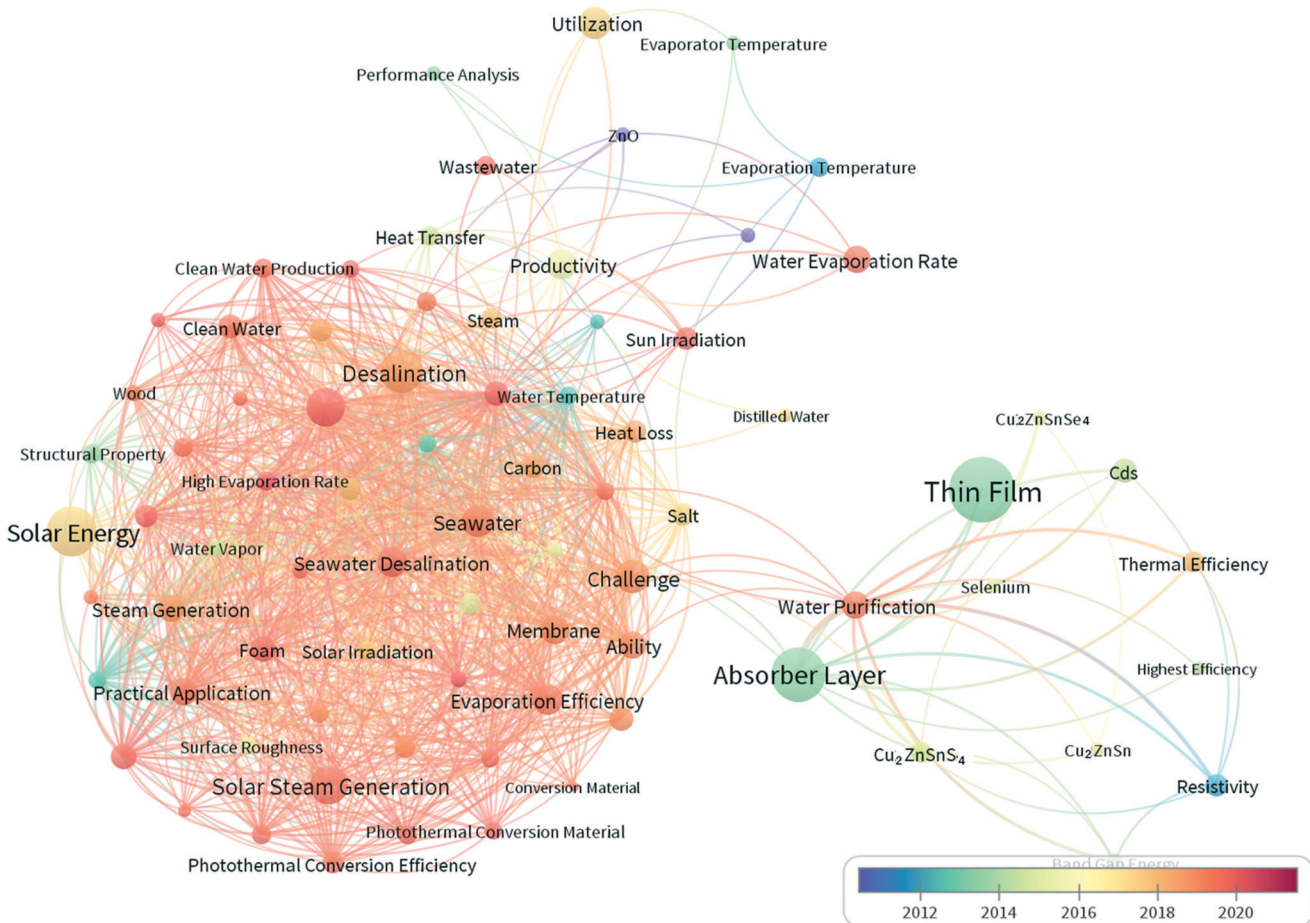


Fig. 1 The network visualization map of co-occurrence keywords for solar evaporation research from 2011 to 2021 (the colors represent the average time of keyword occurrence).

where C is the specific heat capacity of water ($4.2 \text{ kJ kg}^{-1} \text{ K}^{-1}$), \dot{m} is the evaporation rate ($\text{kg m}^{-2} \text{ h}^{-1}$), and T_1 and T_2 are the temperatures of the steam and the bulk water, respectively.

Convection (Q_{conv}) heat loss results from the temperature gradient between the surface of the solar absorber and the surrounding fluid, which is defined by Newton's law of cooling.

$$Q_{\text{conv}} = hA(T_1 - T_2) \quad (3)$$

where h is the natural convective heat transfer coefficient ($\sim 5 \text{ W m}^{-2} \text{ K}^{-1}$),²¹ A is the surface area, and T_1 and T_2 are the temperatures of the solar absorber surface and the surrounding fluid, respectively.²²

Electromagnetic radiation is absorbed and emitted simultaneously by all objects. Radiation heat loss (Q_{radi}) is highly dependent on the temperature and emissivity of materials, which can be defined by the Stefan–Boltzmann equation.

$$Q_{\text{radi}} = \varepsilon\sigma A(T_1^4 - T_2^4) \quad (4)$$

where ε is the emissivity of the absorber surface, σ is the Stefan–Boltzmann constant ($5.67 \times 10^{-8} \text{ W m}^{-2} \text{ K}^{-4}$), and T_1

and T_2 are the temperatures of the absorber surface and surrounding environment.^{16,23}

The performance of solar absorbers can be quantified by the conversion efficiencies of solar-to-thermal or solar-to-steam as follows:

$$\eta_{\text{solar-to-thermal}} = \frac{\alpha Q_{\text{sol}} - Q_{\text{conv}} - Q_{\text{radi}}}{Q_{\text{sol}}} \quad (5)$$

$$\eta_{\text{solar-to-steam}} = \frac{\alpha Q_{\text{sol}} - Q_{\text{conv}} - Q_{\text{radi}} - Q_{\text{cond}}}{Q_{\text{sol}}} \quad (6)$$

where Q_{sol} is the power of solar illumination.²⁴

2.2 Categories of solar evaporation systems

There are four types of solar-driven evaporation systems, which are classified by the location of solar absorbers in the solution. In volumetric heating-based systems (Fig. 4a), heat is generated in the bulk fluid by the well-dispersed solar absorbers, which transfer solar energy to numerous micro-heaters for volumetric heating. In spite of the highly localized heating effect, only moderate vapor generation efficiency (20–60%) can be achieved under one sun (1 kW m^{-2}),^{25,26} due to the occurrence of remarkable radiation, conduction, and

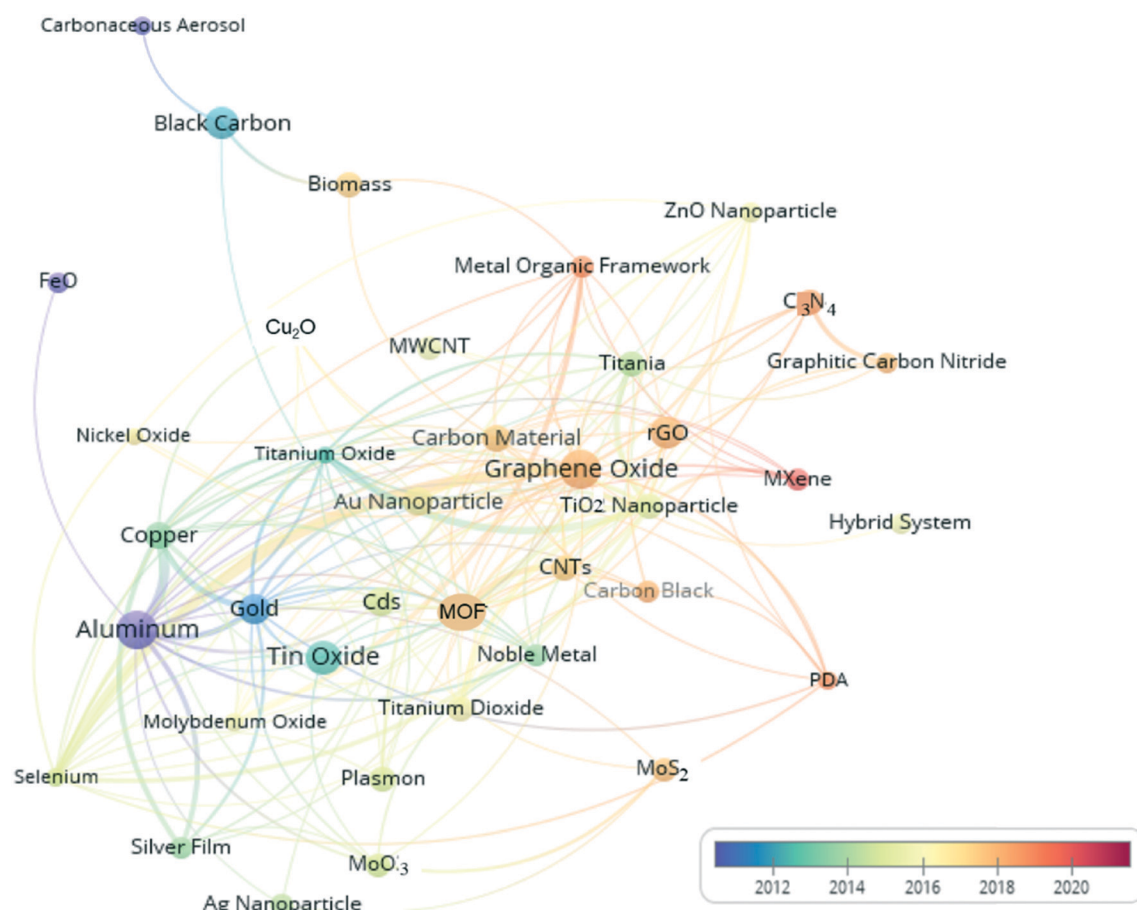


Fig. 2 The network visualization map of co-occurrence keywords for photothermal materials from 2011 to 2021 (the colors represent the average time of keyword occurrence).

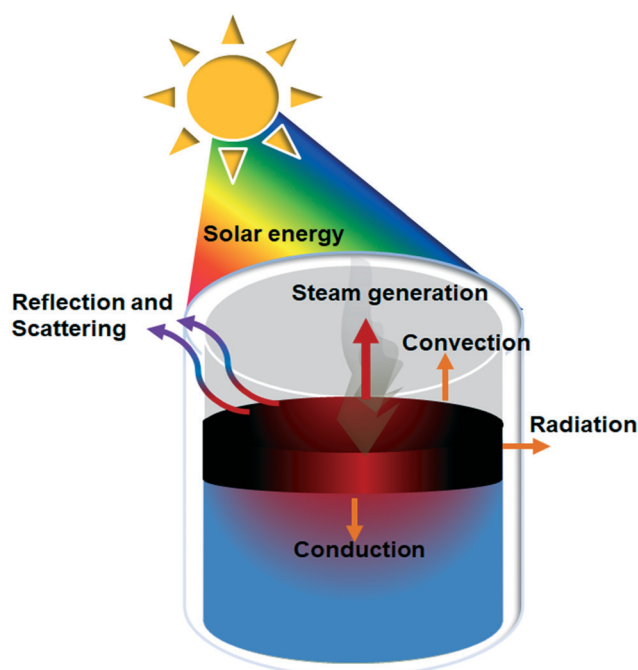


Fig. 3 Energy distribution of an interfacial water evaporation system.

convection heat losses during the bulk water heating. In bottom heating-based systems (Fig. 4b), the solar absorber is located at the bottom of the container to produce heat, whereas vapor generates in a separate site, affording evaporation efficiencies as low as 30–45% due to the extensive heat losses.²⁷ To improve the evaporation efficiency, interfacial heating-based solar evaporation systems are developed (Fig. 4c), in which photothermal conversion and vapor evaporation are located at the air–water interface.²⁸ Taking advantage of the confined thermal energy on the absorber surface, energy loss resulting from the volumetric heating (conduction) can be avoided. Moreover, radiation and convection heat losses are also effectively reduced owing to the lower temperature on the absorber surface resulting from high-efficiency evaporation. As a result, a high solar-to-steam conversion efficiency (~90%) can be achieved under one sun.²¹ However, massive conduction heat loss is inevitable due to the large contact area between the solar absorber and water media. In order to alleviate the heat loss, researchers attempt to isolate the solar absorber from the bulk fluid *via* building up isolation heating-based solar evaporation systems (Fig. 4d). In these cases, water is either transported to the solar absorber through a constructed water channel (Fig. 4d-i) or confined in a sponge (Fig. 4d-ii).¹⁶ In

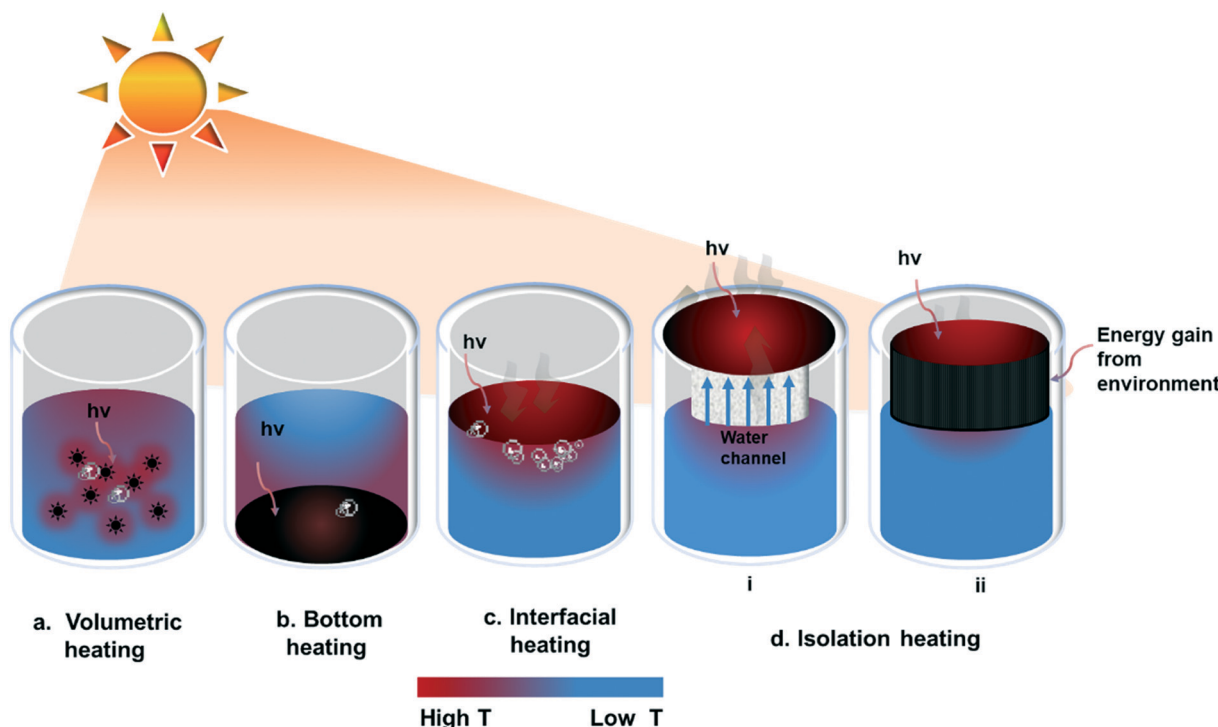


Fig. 4 Categories of solar-driven evaporation systems. (a) Volumetric heating system: solar light is absorbed by uniformly dispersed solar absorbers and transformed into thermal energy to heat the bulk water. (b) Bottom heating system: bulk water is heated by thermal energy converted from solar light via solar absorbers on the bottom. (c) Interfacial heating system: the solar absorber floating on the water surface performs solar-to-thermal conversion at the air–water interface and *in situ* heats the surface water. (d) Isolation heating systems: (i) the solar absorber is separated from bulk water and water is transferred through specific channels; (ii) 3D-structured evaporator with enhanced environmental energy.

particular, the side temperature of the three-dimensional (3D) structure in Fig. 4d-ii is lower than ambient temperature due to evaporation and condensation without heat supplementation by solar absorption. As a result, an extra energy gain from the environment can be achieved, resulting in extremely high energy conversion efficiency beyond 100%.²⁹

In the bottom and volumetric systems, massive unwanted energy losses occur, stemming from the hindered light absorption and water vapor exchange, as well as the unpreventable heat transfer to the bulk water. By contrast, interfacial and isolation evaporation modes are currently more frequently employed, because they can effectively absorb solar radiation and only heat the surrounding local water, which reduces heat dissipation and maximizes light and heat utilization efficiency.³⁰ To compare the performance of these operation modes, He *et al.* loaded the same amount of gold nanoparticles (AuNPs) as solar absorbers in different types of evaporation systems.³¹ They found that the specific steam productivity was in the following order: interfacial system (~85%) > bottom system (~65%) > volumetric system (~50.5%) > bulk water (~20.3%). In contrast, when a 3D nitrogen-enriched carbon sponge was used as the solar absorber material, the isolation system had the highest evaporation rate, solar-to-steam conversion efficiency, and surface temperature among the four types of systems due to the complete localized heating that diminished the heat losses to bulk water.³²

3. Application of solar absorbers in solar evaporation

In general, the photothermal conversion mechanism of solar absorbers can be divided into three categories: plasmonic heating, thermal vibration of molecules, and electron-hole generation/relaxation.²⁵ This review will discuss in detail the recent advances and developments of solar absorbers in solar-driven evaporation systems. On the basis of understanding the underlying mechanism and summarizing their pros and cons, we aim to provide guidance for researchers in terms of the selection and optimization of solar absorbers during construction of solar-driven water evaporation systems.

3.1 Plasmonic heating

When the frequency of incident light matches the oscillation frequency of delocalized electrons in metal nanoparticles (NPs), the collective vibration of electrons is triggered. This phenomenon is so-called localized surface plasmon resonance (LSPR) (Fig. 5a), which is a unique optical phenomenon for metal structures and determines the optical absorption of metal NPs.^{33,34} In the presence of electromagnetic radiation, electrons are excited from an occupied state to an unoccupied state,³⁵ and decay in three different ways (electron-to-photon, electron-to-electron, and

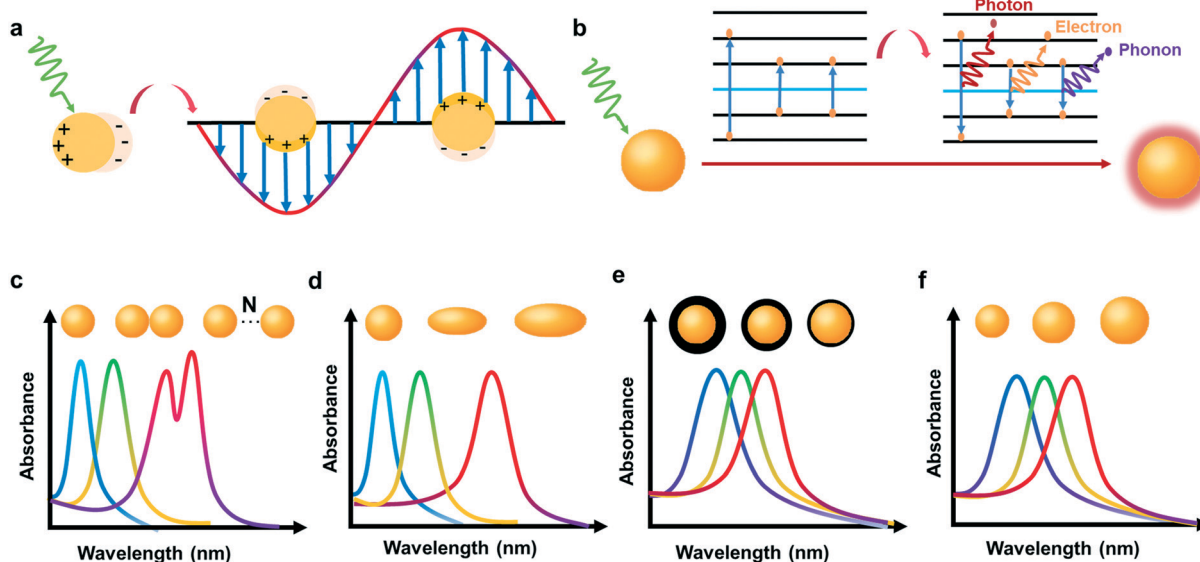


Fig. 5 (a) Schematic diagram of the plasmonic photothermal conversion mechanism. (b) The excitation and decay of electrons produced by plasmonic metals. The effect of plasmonic coupling (c), shape (d), core-shell ratio in plasmonic core–shell structures (e), and size (f) on LSPR absorption.

electron-to-phonon), thereby rapidly increasing the local surface temperature of metal NPs (Fig. 5b).^{36,37} However, most plasmonic metals can absorb light at only one or several particular wavelengths because of their intrinsic narrow extinction bandwidth of LSPR, which hinders their potential application as efficient solar absorbers. In general, geometry, intra/interparticle coupling, and dielectric environment are determinants of the LSPR effect (Fig. 5c–f). For example, the alteration of particle size, aspect ratio, and surrounding dielectric can shift the LSPR band and possibly extend the absorption to a certain degree.^{38,39} Therefore, it is possible to broaden the light absorption range of plasmonic NPs by tuning the size, shape, and assembly configuration, or by constructing plasmonic nanocomposites consisting of NPs with different LSPR absorption values. Various substrate materials, such as the nanoporous alumina template, filter membrane/paper, nickel foam, cellulose microfibers, and melamine sponge, were used to support plasmonic NPs for the improvement of evaporation performances. In this section, we summarized the performance of plasmonic NPs in solar evaporation (Table 1).

3.1.1 Precious metal NPs. Among the precious metal NPs, gold (Au) and silver (Ag) NPs are commonly used as photothermal agents due to their chemical stability, tunable size, shape and optical properties, and ease of synthesis. More importantly, their LSPR peaks are in the vis-near infrared (NIR) region. Like other metal NPs, precious metal NPs exhibit strong plasmon resonance absorption only in a specific spectral range. In order to improve their photothermal performance, two strategies are commonly used. One is to adjust the particle size and shape to expand the LSPR spectral range.⁴⁰ The other is to generate plasmonic coupling by hybridizing the resonance modes of two

plasmonic NPs,⁴¹ which can result in the redshift and widening of the resonance band.⁴²

Owing to the small Drude damping factor of Au, the absorption band of spherical or cubic AuNPs is restrained to a narrow width, making it difficult to match the solar spectrum.⁴³ Neumann *et al.* are pioneers of using dispersing AuNPs as solar absorbers for water evaporation.^{25,44} Although only a limited solar-to-steam generation efficiency (24%) was achieved, this work motivated researchers to explore the potential application of AuNPs in solar-driven evaporation. Since then, a series of efforts have been made to enhance the photothermal conversion efficiency of AuNPs. By increasing the particle size in the range of 3 to 40 nm, the photothermal conversion efficiency of AuNPs was increased because of the redshift of the absorption band and enhancement of the absorption intensity.⁴⁰ Another way to improve the photothermal conversion is to broaden the LSPR spectral range by modulating the particle shape. In contrast to spherical AuNPs that have only a single absorption peak, anisotropic gold nanorods (AuNRs) have two characteristic LSPR absorption bands. The one at shorter wavelength is caused by the plasmon oscillation along the short axis of the nanorods, while the other at longer wavelength results from the longitudinal plasmon oscillation (along the long axis). The increase of AuNPs' aspect ratio can induce the redshift of long axis LSPR, enhancing the absorption intensity.^{45,46} The heating efficiency could be increased by ~60% from spherical to nanorod (aspect ratio 3 : 1).⁴⁷ In addition, altering the dielectric environment by dielectric coating on AuNPs or constructing a dielectric core–gold shell nanostructure can also induce the redshift of the LSPR band, even from the visible to NIR region.^{48,49} However, the high price of AuNPs limits their practical application in solar evaporation.

Table 1 Properties, parameters, and performance of plasmonic material-based solar evaporators

| Solar absorbers | Particle size (nm) | Pore size (μm) | Power density (kW m^{-2}) | Wavelength range (nm) | Absorption (%) | Solar-thermal efficiency (%) | Solar-steam efficiency (%) | Evaporation rate ($\text{kg m}^{-2} \text{ h}^{-1}$) | Thermal conductivity ($\text{W m}^{-1} \text{ K}^{-1}$) | Stability/scalability | Surface property | Ref. |
|---|---|-----------------------------|--------------------------------------|-----------------------|----------------|------------------------------|----------------------------|--|---|-----------------------|------------------|------|
| AuNPs deposited on AAO membrane | Random | 0.3 | 4 | 400–10000 | ~99 | — | 90 | ~5 | — | — | — | 98 |
| Black Au-coated Al nanowires | — | ~0.15 | 20 | 400–2500 | 91 | 57 | — | 15.95 | — | — | Hydrophilic | 99 |
| AgNPs | 48.7–411.9 | — | 0.3–0.967 | 300–1400 | — | 82.45 | — | 1.008 | — | 15–16 months | — | 38 |
| Black AgNPs | — | — | 1 | 400–1000 | — | — | 95.2 | 1.38 | — | 10 cycles | — | 42 |
| AlNPs deposited on AAM | — | — | 4 | AM1.5G | 96 | — | 88.4 | ~5.7 | — | 25 cycles | — | 55 |
| CuNPs | ~50 | — | 2 | 200–1300 | ~97.7 | 93 | 73 | ~1 | — | Stable/scalable | — | 59 |
| HCS NW | — | — | 1 | 200–2500 | 93 | — | 86 | 1.37 | — | 310 days | Hydrophobic | 100 |
| NF | — | — | 1 | 250–2500 | ~90 | 94 | — | 1.41 | 0.243 | 25 cycles | Hydrophilic | 64 |
| Ni NPs | ~12 | — | 1 | 200–2500 | 97.1 | 81.8 | 79.3 | ~1.2 | — | 10 days/scalable | — | 24 |
| Te–Se nanomaterial | A major axis 85–170 nm; a minor axis of 40–110; a | 1 | 300–2500 | 93–95 | — | 86.14 ± 1.02 | 1.323 ± 0.015 | — | — | Stable | Hydrophilic | 67 |
| Ti ₃ C ₂ MXene | — | 5–35 | 1 | 200–2500 | 96 | ~100 | 87 | 1.46 | — | 15 days/scalable | Hydrophobic | 73 |
| TiN loaded on CW | 40 | — | 5 | 200–1800 | — | 80 | 44 | 8.8 | — | — | Hydrophilic | 101 |
| WO _{3-x} NR-decorated wood | 10 | — | 1 | 200–1800 | 94 | — | 82.5 | 1.28 | — | 60 cycles | Hydrophilic | 83 |
| CZTS nanosheet-assembled membranes | 10–20 | 0.1–0.6 | 1 | 200–2500 | 92.25 | — | 84.5 | 1.46 | 0.002 | 20 h/scalable | — | 96 |
| Cu ₂ SnSe ₃ (or Cu ₂ ZnSnSe ₄) nanosphere arrays | 300–500 | — | 1 | 250–2500 | >95 | 86.6 | 85.7 | 1.657 | — | 15 days/scalable | Hydrophobic | 97 |

Due to the much higher plasmonic resonance response, the heat generation of AgNPs is ten times stronger than that of AuNPs.⁵⁰ In addition, AgNPs are cheaper, making them promising alternatives to AuNPs in solar evaporation.³⁸ Similar to AuNPs, the narrowband absorption of AgNPs can only match a small part of the solar spectrum and researchers also make efforts to optimize their size and shape.⁵¹ For example, Miao *et al.* synthesized Ag polyhedral quasi-spheres with diameters ranging from 48.7 to 411.9 nm.³⁸ As the size increased, the plasmonic peaks involving dipole modes were red-shifted accompanied by the emergence of new peaks due to multipole modes. This result is consistent with Mie theory, meaning that NPs with smaller size only show a dipole plasmonic peak, while larger ones have dipole and multipole plasmonic peaks.^{51,52} As a result, the LSPR absorption of AgNPs was well matched to the solar spectrum.

Wang *et al.* synthesized black Ag nanostructures with well-distributed interparticle distance by a unique confined seed growth strategy.⁴² By fixing the seeds in a confined rod-shaped tubular space, the distance between particles could be gradually reduced as the seeds grew, thereby generating

random plasmonic coupling that is responsible for the broadband absorption. Importantly, the energy conversion was improved by the multi-reflection process in the porosity of AgNP assemblages (Fig. 6a). By depositing the Ag nanostructures on filter paper, black Ag films were fabricated for interfacial solar evaporation, showing a steam generation efficiency as high as 95.2%. However, the potential risk of toxic Ag⁺ release should be considered when AgNPs are applied in solar evaporation.

3.1.2 Other metal NPs. The high cost of solar absorbers is one of the main limitations for the development of large-scale solar evaporation. Therefore, solar absorbers with low price, such as aluminum (Al, US\$1000 per ton), are desirable candidates.⁵³ Since Al shows strong plasmonic response in the UV region, it is challenging, but essential to broaden it towards the IR range for efficient solar-to-thermal conversion. It has been reported that the intrinsic oxidation of Al can redshift and broaden the LSPR absorption of Al-based systems by altering the effective dielectric surroundings.⁵⁴ In view of this concept, Zhu *et al.* constructed a plasmonic-enhanced light absorber by assembling Al NPs into a 3D nanoporous anodized aluminum oxide membrane (AAM). Al

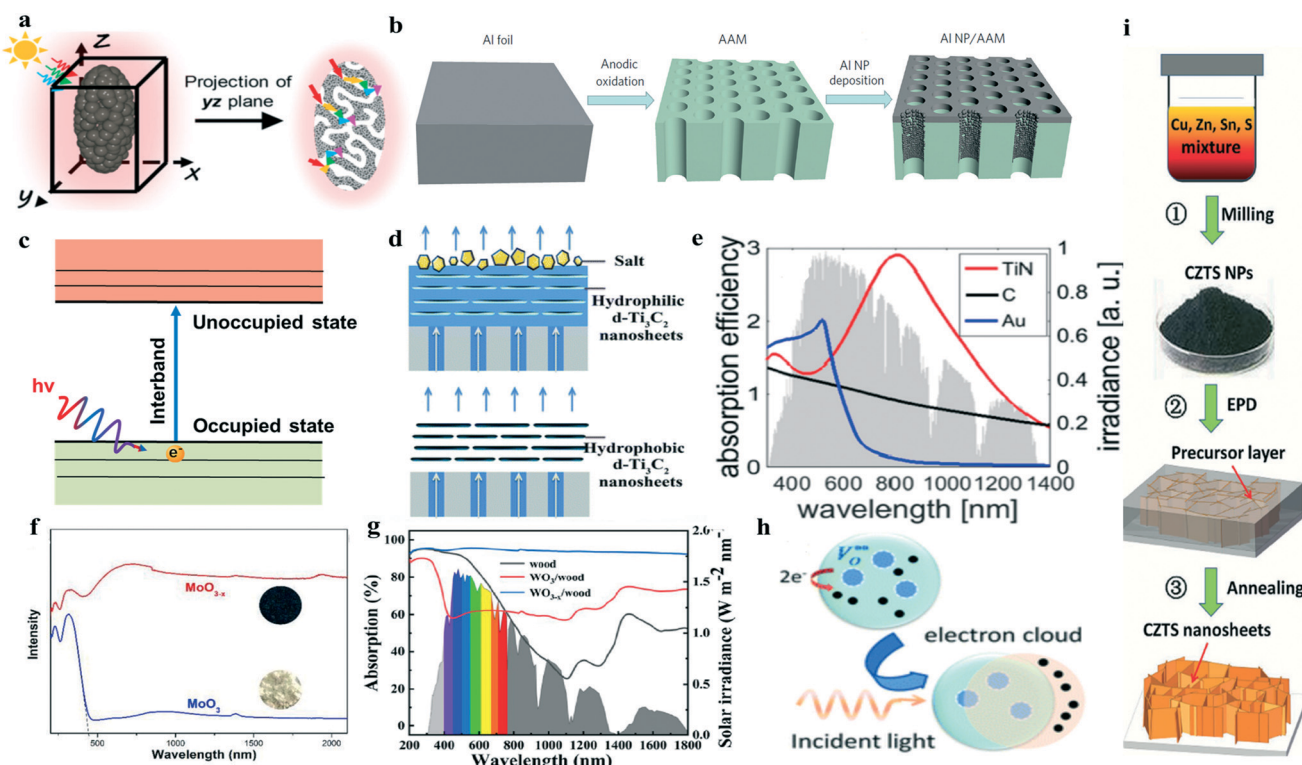


Fig. 6 (a) Schematic diagram of the light path in the AgNP assemblage. Reprinted with permission from ref. 42 Copyright 2019, American Chemical Society. (b) Schematic diagram of the fabrication process of the Al NP-based plasmonic structure. Reprinted with permission from ref. 55 Copyright 2016, Nature Publishing Group. (c) Schematic illustration of IBTs: the electron transitions from an occupied state to an unoccupied state after being excited by light. (d) Schematic diagram of the solar evaporation process for hydrophilic and hydrophobic membranes. Reprinted with permission from ref. 75 Copyright 2018, Royal Society of Chemistry. (e) Calculated absorption efficiencies of aqueous dispersions of TiN, carbon, and Au nanospheres with a radius of 50 nm. Reprinted with permission from ref. 43 Copyright 2016, American Chemical Society. (f) UV-vis-NIR diffuse reflectance spectra of MoO₃ and MoO_{3-x}. Reprinted with permission from ref. 89 Copyright 2019, Royal Society of Chemistry. (g) Absorption of pure wood and WO₃/WO_{3-x}-decorated wood evaporators. Reprinted with permission from ref. 83 Copyright 2020, Elsevier BV. (h) Schematic diagram of the LSPR generation process by oxygen vacancies in TiO_{1.67} NPs. Reprinted with permission from ref. 84 Copyright 2016, Royal Society of Chemistry. (i) Schematic diagram of the preparation process of the self-assembled CZTS nanosheets. Reprinted with permission from ref. 96 Copyright 2017, Wiley.

NPs were then deposited on the AAM to form a thin film (Fig. 6b),⁵⁵ which achieved broadband solar absorption (>96%) and efficient energy conversion (~90%). In addition to the intrinsic oxidation-induced redshift and broadening of LSPR absorption, there were several other reasons contributing to the wide solar absorption. First, Al NPs were tightly aligned within the AAM along the pore walls, which induced strong plasmonic hybridization and LSPR effects. Moreover, Al showed stronger plasma frequency than precious metals due to the ohmic damping and near-field enhancement, thus promoting the plasmonic absorption.⁵⁶ In addition, the porous AAM could effectively reduce the surface reflection and increase the internal light scattering, which further enhanced the total absorption.⁵⁷

Compared to AuNPs and AgNPs, copper NPs have LSPR peaks at longer wavelength due to their strong vis-NIR absorption and omnidirectional light absorption properties.⁵⁸ Within a broad incident angle (0 to 50°), a near-unity light absorption (~97.7%) and high photothermal conversion efficiency (93%) in the wavelength range of 200 to 1300 nm were achieved.⁵⁹ Since the incident sunlight covers all directions, the unique omnidirectional photothermal conversion capacity is desirable for solar absorbers.

Interband transition (IBT) is another light absorption mechanism for metals (Fig. 6c). Different from the coherent excitations of electrons for plasmonic absorption, individual electrons in occupied states in one band are excited to unoccupied states in another band for IBTs when the photon energy exceeds the interband threshold of a metal, so that IBTs have broadband optical response.⁶⁰ The IBTs of transition metals, such as Ni, Pd, and Pt, cover the full-spectrum solar light due to the high density of electronic states (DOS) near their Fermi levels, which are in favor of the utilization of the entire solar energy.^{61,62} As a result, although nickel (Ni) is not considered as a strong plasmonic material as Au, Ag, and Cu,⁶³ it has strong solar harvesting capacity. Moreover, Ni has superior chemical stability (better than Al and iron), promoting the exploration of its potential application in solar evaporation. Qu *et al.* constructed a nanostructured Ni–NiO_x/Ni foam (NF), composed of Ni NPs and defective NiO_x.⁶⁴ Due to the plasmonic effect of Ni NPs and the rich defects of NiO_x, Ni–NiO_x/NF showed broadband light absorption, with an average solar conversion efficiency of 94%. In addition, the low thermal conductivity of Ni–NiO_x/NF (0.243 W m⁻¹ K⁻¹) could effectively prevent heat loss to surrounding media, ensuring a high evaporation rate (1.41 kg m⁻² h⁻¹). Nevertheless, Ni is prone to oxidation, which compromises the plasmonic property, thus restricting its application in real-life.

Yang *et al.* first demonstrated that tellurium (Te) exhibits plasmonic-like and high-index all-dielectric properties in the solar radiation region. According to the particle size, the mechanisms can be classified into quasi-static resonance (<120 nm) and Mie-type resonance (>120 nm). Combining the advantages of plasmonic and all-dielectric nanostructures in photothermal conversion, an absorber composed of Te

NPs can absorb more than 85% of the energy in the entire solar spectrum.⁶⁵ In spite of its superior optical property, Te is known as a waterborne pollutant and may be harmful to the aquatic environment and human health.⁶⁶ In order to overcome these disadvantages, a layer of selenium (Se) shell was coated on Te NPs, which could not only prevent the Te core from oxidizing, but also improve the biocompatibility of the core-shell nanostructures.⁶⁷ This work opens up possibilities for the application of Te-based solar absorbers in solar evaporation, wastewater treatment, and photothermal therapy.

3.1.3 MXene. MXene, a new class of two-dimensional (2D) materials containing transition metal carbides, nitrides, and/or carbonitrides, was first developed by the group of Gogotsi in 2011.⁶⁸ Their chemical formula is M_{n+1}X_nT_x, where M is an early transition metal, X is carbon and/or nitrogen, and T_x is the surface functional group.^{69,70}

As the most studied MXene, titanium carbide (Ti₃C₂) is originally used as an electromagnetic interference shielding material. The electromagnetic waves absorbed by Ti₃C₂ are emitted in the form of heat due to the LSPR effect derived from the semimetal character of Ti₃C₂,⁷¹ which inspires researchers to explore the photothermal conversion performance of Ti₃C₂. Wang *et al.* found that Ti₃C₂ exhibited outstanding internal photothermal conversion efficiency (100%) at wavelengths of 473 and 785 nm.⁷² The stacked MXene film was subjected to an evaporation experiment and presented an evaporation efficiency of 84%. Since then, Ti₃C₂-based solar evaporation has been extensively studied.^{73,74} By filtrating the trimethoxy(1H,1H,2H,2H-perfluorodecyl)silane (PFDTMS) modified Ti₃C₂ nanosheets on a commercial filter membrane, a hydrophobic MXene membrane was obtained.⁷⁵ The desalination performance was inspiring, with an evaporation rate of 1.31 kg m⁻² h⁻¹ and steam conversion efficiency of 71% under one sun. The hydrophobic Ti₃C₂ membrane acted as a solvent barrier to block the passage of salt, which contributed to the prolonged stability (200 h) during concentrated seawater desalination (Fig. 6d). Some other transition metal carbides (TMCs), such as Nb₂C and Ta₄C₃, also showed remarkably high photothermal conversion efficiency and satisfactory performance in phototherapy.^{76,77} Hence, it is possible to expand the application of the 2D MXene family in solar evaporation.

Another class of MXene is transition metal nitrides (TMNs), such as titanium nitride (TiN) and zirconium nitride (ZrN), which show plasmonic character in the vis-NIR region because of their zero crossover wavelength of dielectric permittivity in the visible range analogous to Au.⁷⁸ They have stronger broadband light absorption, lower cost, and higher temperature durability than precious metals. The average absorbance of TiN NPs in the range of 400–800 nm is greater than 95%.⁷⁹ In contrast to Au and black carbon NPs, TiN NPs with comparable size at the same concentration showed higher solar absorption efficiency.⁴³ Compared to the sharp peak of Au NPs at ~530 nm, a broad LSPR peak of TiN NPs was observed at ~700 nm because of the lossy plasmon resonances (Fig. 6e).^{43,80} Although carbon and TiN NPs had a

similar absorption span, the light absorption efficiency of TiN NPs was higher than that of carbon NPs throughout the record wavelengths. Importantly, the absorption curve of TiN NPs overlapped well with the solar spectrum, meaning that solar energy can be effectively harvested by TiN NPs.⁴³ These results inspire researchers to explore the application of other TMNs with dielectric functions similar to TiN in solar evaporation.

3.1.4 Plasmonic semiconductors. Unlike precious metals, whose LSPR needs to be adjusted through complex shape or size control, plasmonic semiconductors can be endowed with excellent LSPR property in the visible-NIR region through the enhancement of free charge carriers either by self-doping to form cation vacancies, or by doping with heterovalent dopant atoms.^{81,82} In addition, they also possess photocatalytic property, which provides an opportunity to combine solar evaporation and photocatalytic degradation for wastewater treatment.

The creation of oxygen vacancies or interstitials *via* aliovalent doping provides metal oxides with metallic behavior by stabilizing a large number of charge carriers.⁸¹ Oxygen-deficient metal oxides, such as MoO_{3-x} , WO_{3-x} and $\text{TiO}_{1.67}$, exhibit excellent LSPR absorption in near- and mid-infrared wavelengths due to the unique characteristics of their outer-d valence electrons.^{83,84} In recent years, WO_{3-x} and MoO_{3-x} have been widely used as photothermal and photodynamic agents for cancer therapy due to their outstanding light absorption and photothermal conversion properties.^{85,86} Interestingly, it is possible to tune the LSPR to match the solar spectrum by manipulating the oxygen-deficient stoichiometries.^{87,88} As shown in Fig. 6f, MoO_3 only can be excited by UV-vis light with the band edge at ~ 443 nm due to its wide band gap (~ 2.8 eV).⁸⁹ In contrast, the absorption of oxygen-deficient MoO_{3-x} was extended to the IR region due to the narrowed band gap.

Cui *et al.* used WO_{3-x} nanorods (NRs) as light-absorbing materials and assembled them on the surface of wood.⁸³ In the spectral range of 200–1800 nm, the light absorption of the WO_{3-x} NR-decorated wood evaporator (94.0%) was much higher than that of the WO_3 NR-decorated wood evaporator (67.4%) (Fig. 6g). This is because the tunable LSPR of oxygen-deficient WO_{3-x} NR greatly broadened the absorption range from the visible region to vis-NIR regions. Yang *et al.* synthesized self-doped $\text{TiO}_{1.67}$ with a large amount of oxygen vacancies.⁸⁴ Under incident light radiation, a large number of electrons generated by oxygen vacancies will form an oscillating electron cloud, resulting in LSPR (Fig. 6h). When the LSPR energy is higher than the band gap due to the adequate self-doping density, the interband plasmon resonances occur, allowing the emergence of much more hot carriers in $\text{TiO}_{1.67}$ NPs for efficient light harvesting and heat generation.^{90,91} In addition to the oxygen-deficient metal oxides, some other doped metal oxides, such as rubidium tungsten bronze (Rb_xWO_3),⁹² hydrogenated metal oxide ($\text{H}_{1.68}\text{MoO}_3$),⁹³ and defective HNb_3O_8 ,⁹⁴ also exhibit quasi-metallic properties and excellent light absorption and

photothermal conversion capabilities, providing the possibilities for application in solar evaporation.

Besides doped metal oxides, copper-deficient copper chalcogenides, including Cu_{2-x}S , Cu_{2-x}Se , $\text{CuXS}_2/\text{Se}_2$ (X = Al, Ga, In), and $\text{Cu}_2\text{ZnSnS}_4/\text{Se}_4$, are also plasmonic semiconductors, with the absorbance range of 800–1200 nm.⁹⁵ In these self-doped semiconductors, the free holes induced by cation vacancies contribute to LSPR. Song *et al.* prepared microporous CZTS films with typical plasmonic nanostructures (Fig. 6i),⁹⁶ which showed high light absorption ($\sim 92.25\%$) in the solar spectrum (200–2500 nm) due to the LSPR effect of the CZTS semiconductor.⁹⁷

3.2 Thermal vibration of molecules

Generally speaking, once photons are absorbed, a molecule can be excited and rapidly converted to the lowest excited singlet state (S_1). Because of the excess energy, the excited state undergoes deexcitation, including radiative emission (fluorescence), thermal vibration (non-radiative relaxation), and intersystem crossing, to decay back to the ground state (Fig. 7a). Among them, non-radiative relaxation plays a dominant role in the photothermal effect. When oxygen-containing functional groups are introduced, non-radiative recombination of light-irradiated electrons is induced, which can promote fluorescence quenching and heat release.¹⁰² For carbonaceous materials and some conjugated polymers (*e.g.*, polypyrrole and polydopamine), although the transition from σ to σ^* is impossible under solar light due to the large energy gaps, the loosely bonded electrons in the π orbital can be easily excited to the π^* orbital with a smaller energy input, especially when the π bonds are conjugated, which induces the red-shift of the absorption spectrum and further narrows the energy gap between the ground state (highest occupied molecular orbital, HOMO) and the excited state (lowest unoccupied molecular orbital, LUMO). The excited electrons are relaxed by electron-phonon coupling, thereby generating lattice vibration, which facilitates the photothermal conversion (Fig. 7b).^{9,11} In this section, we summarized the solar evaporation performance of carbonaceous materials, conjugated polymers, and small organic molecules that conduct solar-to-thermal conversion *via* thermal vibration of molecules (Table 2).

3.2.1 Carbonaceous materials. The emissivity of carbonaceous materials is limited to ~ 0.85 due to the moderate reflection (5–10%) at the air-dielectric interface.¹⁰⁴ It is difficult to enhance the light absorption by lowering their intrinsic reflectance. Fortunately, the reflective energy loss can be reduced by extending the optical path length through trapping incident light in the nanostructure, which improves the light absorption by multiple internal reflections.^{105,106} Based on the principle, researchers have developed a series of nanostructures with different geometries, including vertically-aligned, porous, and hierarchical structures (Fig. 7c–e),¹⁰³ for efficient solar light harvesting during water evaporation.

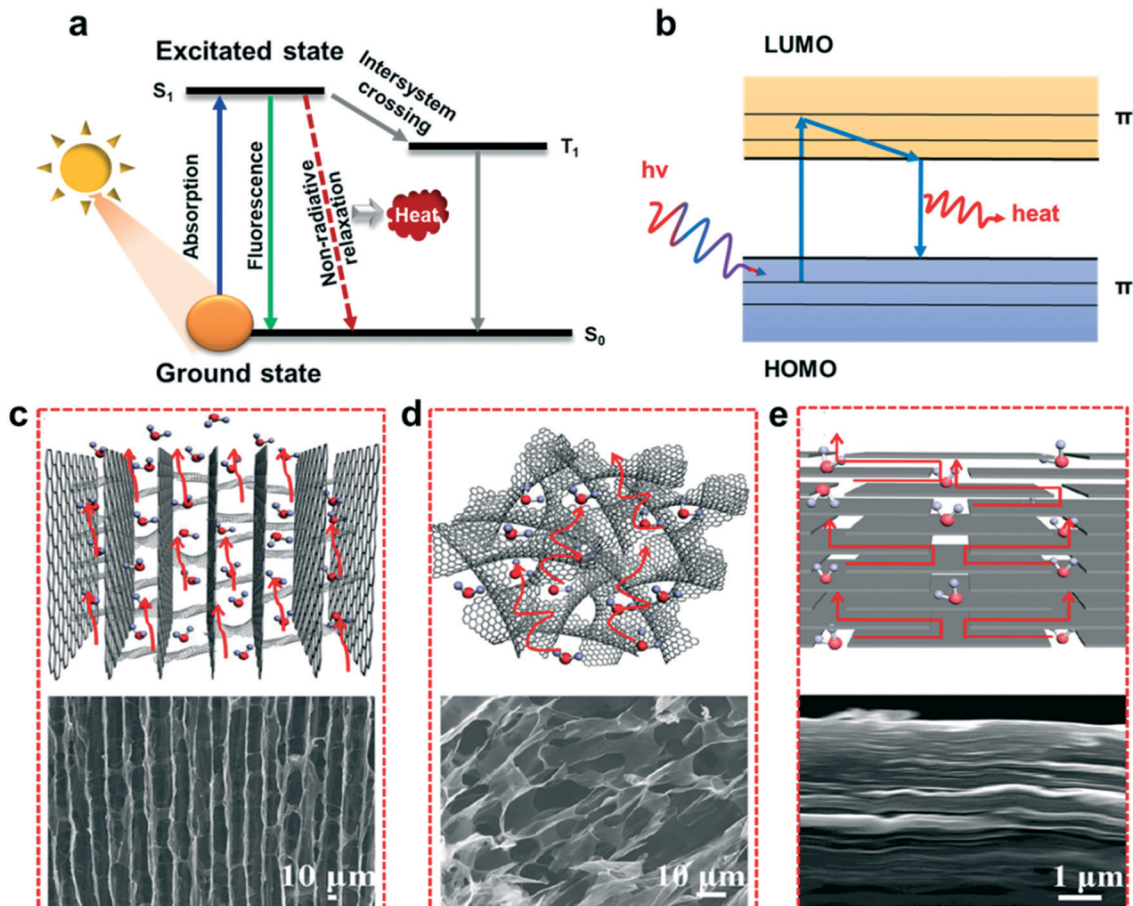


Fig. 7 (a) Illustration of the energy transformation of organic molecules. (b) Photothermal conversion mechanism via thermal vibration of molecules. Geometries of carbonaceous material-based nanostructures: vertically-aligned (c), porous (d), and hierarchical (e) structures. Reprinted with permission from ref. 103 Copyright 2017, American Chemical Society.

Since Ghasemi pioneered the use of graphene in solar distillation in 2014,²¹ researchers have been committing to manipulating the architecture of graphene-based evaporators to improve the evaporation efficiency. Qu's group prepared vertically-aligned graphene films (VA-GSM) by the antifreeze-assisted freezing technique (Fig. 8a), which facilitated water supply, steam escape, and broadband absorption (93% of UV, 98% of visible, and nearly 100% of NIR light).¹⁰³ As a result, an average water production rate of $1.62 \text{ kg m}^{-2} \text{ h}^{-1}$ and photothermal conversion efficiency of 86.5% were achieved under one sun. Apart from graphene, Qu's group also explored the potential of rGO as a light absorber. To mitigate the high thermal emittance (>95%)-induced heat loss of carbon-based materials, they prepared a rGO-based spectral selective absorber (rGO-SSA) composed of an Al substrate, multilayer rGO film, and silica NP layer (antireflection coatings, ARC) by thermal reduction (Fig. 8b).¹⁰⁷ Thanks to the lossy constructive interference in the rGO film resulting from the structural alteration during thermal reduction of GO to rGO (Fig. 8c), rGO-SSA showed an extremely low thermal emissivity ($\varepsilon_{100} \approx 0.04$) and a high solar absorptance ($\alpha_{\text{solar}} \approx 0.92$) (Fig. 8d). Other graphene family materials, including graphite-derived carbon dots,¹⁰⁸ GO,^{109,110} and

EGr,^{108,111} are also applicable in solar evaporation. In addition, functionalization of graphene with hydrophilic groups (e.g., -OH and -COOH) was demonstrated to improve the solar-to-vapor efficiency.¹¹² Inspiringly, doping graphene with nitrogen atoms can decrease the thermal conductivity, total reflectance, and transparency, which is in favor of maximizing the photothermal conversion efficiency.¹¹³ Aside from solar energy utilization efficiency, salt accumulation, and heat loss, cost is also a critical issue that may limit the practical and large-scale applications of solar evaporation. Our group is committed to maximizing the utilization efficiency and reducing the dosage of photothermal layered graphene for economic feasibility.¹¹⁴

Carbon nanotubes (CNTs) have been used as desirable solar absorbers, since they possess broadband solar absorptance, high solar-to-thermal conversion efficiency, low specific heat capacity, and high stability. In spite of the limited emissivity, when the vertical aligned CNTs (VACNTs) were arranged to form a 3D forest-like structure, nearly perfect absorption (98–99%) across a wide range of solar spectrum (200–200 000 nm) was obtained, making them the darkest material in the world.^{104,115} Taking advantage of the attractive photothermal property, Zhang *et al.* for the first

Table 2 Properties, parameters, and performance of carbonaceous material-based solar evaporators

| Solar absorbers | Power density (kW m^{-2}) | Wavelength range (nm) | Absorption (%) | Solar-thermal efficiency (%) | Solar-steam efficiency (%) | Evaporation rate ($\text{kg m}^{-2} \text{ h}^{-1}$) | Thermal conductivity ($\text{W m}^{-1} \text{ K}^{-1}$) | Stability/scalability | Surface property | Ref. |
|------------------------|--------------------------------------|-----------------------|-----------------------------------|------------------------------|----------------------------|--|---|-----------------------|------------------|------|
| VA-GSM | 1 | 250–2500 | 93% UV; 98% vis; 86.5 100% NIR | — | — | 1.62 | 0.0038 | Stable/scalable | Hydrophilic | 103 |
| HOPGF | 1 | 250–2500 | 98–98.5 | 95 | — | 2.1 | 0.018–0.035 | Scalable | Hydrophilic | 165 |
| PGS/GF | 1 | 250–2500 | 97.4 | 91.7 | — | 2.01–2.61 | 0.051 | 8 h/scalable | Hydrophilic | 166 |
| rGO-SSA | 6 | 250–2500 | 92 | — | — | — | — | 800 °C/scalable | — | 107 |
| rGO foam | 1 | 200–2500 | 98 | 99.4 | — | 2.4 | 0.05 | Stable | Hydrophilic | 167 |
| VACNT | 15 | 280–820 | 99 | — | 90 | ~16 | — | — | Hydrophilic | 116 |
| F-Wood/CNTs | 10 | 300–1200 | 98 | — | 81 | 11.22 | 0.21 | 20 cycles/scalable | Hydrophilic | 117 |
| CB/PMMA–PAN | 1 | 200–2500 | 97 | — | 72 | 1.3 | 0.0392 | 16 days/scalable | Hydrophobic | 121 |
| Carbonized | 1 | 400–1200 | 96 | — | 87.3 | 1.27 | 0.02856 | — | — | 168 |
| MFs | — | — | 92 | — | 1.98 | 0.56 | 15 cycles/scalable | Hydrophilic | 169 | |
| AMS | 1 | 250–2500 | 99 | — | 80.4 | 11.2 | 0.2 | 25 cycles/scalable | Hydrophilic | 124 |
| Carbonized wood | 10 | 250–2500 | 99 | — | — | — | — | — | Hydrophilic | 124 |
| Carbonized mushrooms | 1 | 200–2500 | 96 | — | 78 | 1.475 | 0.45 | 8 cycles | Hydrophilic | 126 |
| Carbonized rice straws | 1 | 200–2500 | 89.4 | — | 75.8 | 1.2 | 0.5 | 14 days/scalable | Hydrophilic | 127 |
| FW-based evaporators | 1 | 300–2500 | 90 | — | 84.1 | 1.3 | — | — | Hydrophilic | 128 |
| PPy-coated meshes | 1 | — | — | — | 58 | 0.92 | — | 100 h | Hydrophobic | 142 |
| PPy/PVA | 1 | 250–2000 | — | — | 94 | 3.2 | — | 28 days/scalable | — | 145 |
| CMP | 1 | 200–2500 | 99 | — | 81–86.8 | ~1.4 | 0.192–0.022 | Stable | Hydrophobic | 159, |
| TQC | 1 | 250–2500 | — | — | 90.3 | 1.67 | — | 6 cycles | — | 160 |
| AFA | 1 | 200–2500 | ~90 | — | 86.5 | 1.43 | — | Stable | Hydrophilic | 163 |

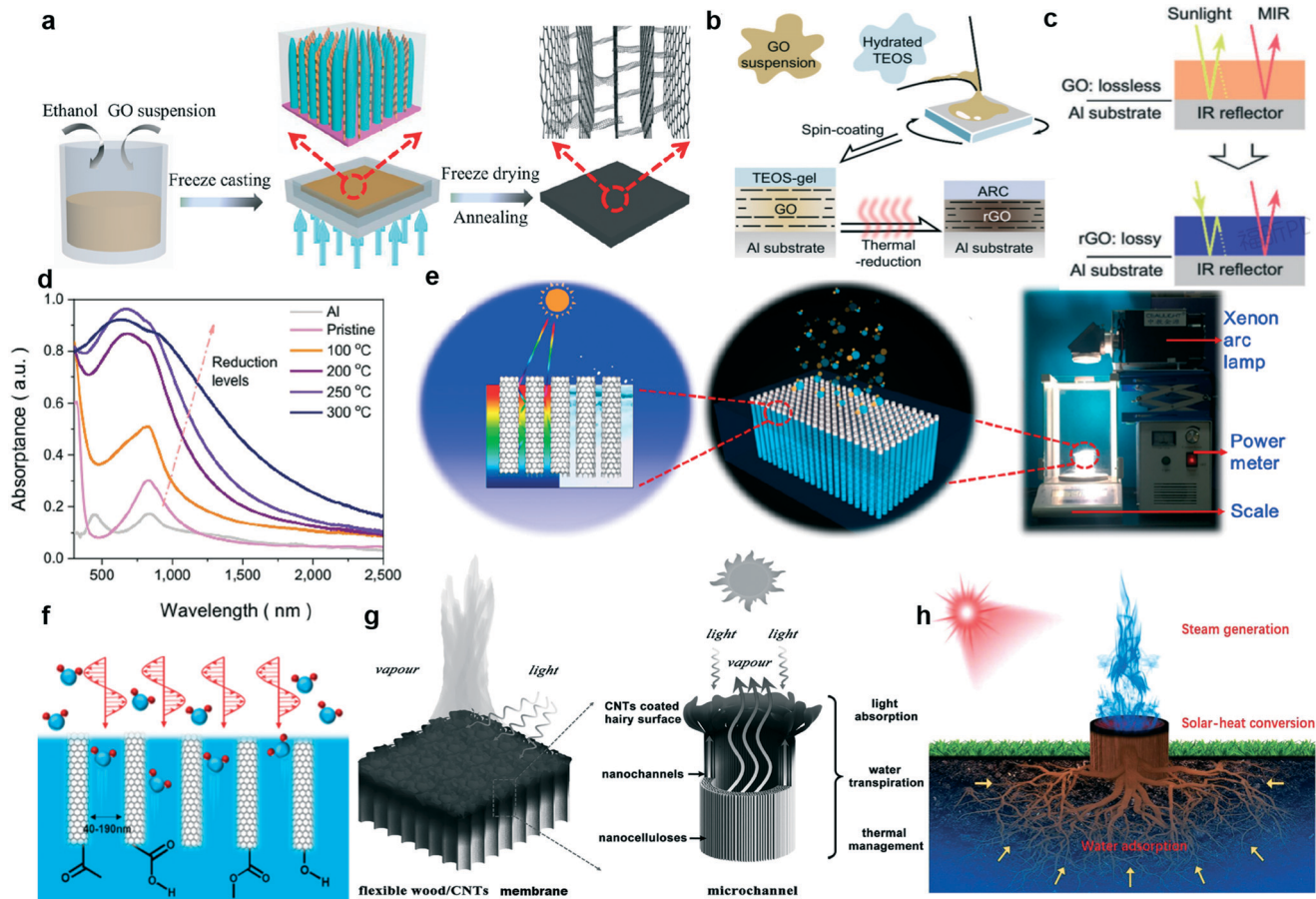


Fig. 8 (a) Preparation of VA-GSM by the antifreeze-assisted freezing technique. Reprinted with permission from ref. 103 Copyright 2017, American Chemical Society. (b) Fabrication process of rGO-SSA by a two-step sol-gel spinning process. (c) Schematic diagram of lossless and lossy interferences in GO and rGO films, respectively. (d) Absorption spectra of the rGO film reduced at different temperatures. Reprinted with permission from ref. 107 Copyright 2020, Wiley. (e) Schematic diagram of the equipment VACNT-based device for solar evaporation. (f) Schematic diagram of the intimate contact between water and VACNTs for efficient heat transfer and water evaporation. Reprinted with permission from ref. 116 Copyright 2017, American Chemical Society. (g) Schematic structure of the F-Wood/CNTs membrane composed of the CNT coated hairy surface for sunlight absorption, micro- and nano-channels for water pumping, and low thermal conductive wood for heat insulation. Reprinted with permission from ref. 117 Copyright 2017, Wiley. (h) Graphical illustration of the groundwater solar steam generation device based on a tree plant. Reprinted with permission from ref. 118 Copyright 2019, Wiley.

time used VACNT for solar evaporation (Fig. 8e).¹¹⁶ Up to 99% of the solar energy in the wavelength range of 280–820 nm was absorbed due to the sparsity and imperfect alignment of vertical single-walled CNTs.¹¹⁵ The hydrophilic surface is conducive to intimate contact between water and the VACNT array and efficient heat transfer (Fig. 8f), thus achieving a high solar-thermal conversion performance (90%). Inspired by the transpiration process of natural plants, Hu's team coated CNTs on the flexible wood with a hair-like surface to construct the F-Wood/CNTs membrane (Fig. 8g).¹¹⁷ The F-Wood/CNTs membrane exhibited extremely low transmittance (<1%) and reflectivity (~2%) in the vis-NIR wavelength range (300–1200 nm) with light absorption as high as 98%. Afterwards, they proposed a new strategy to extract clean water directly from groundwater by coating a root-bearing tree stump with a thin layer of CNTs (Fig. 8h).¹¹⁸ This work offers an efficient and energy-saving method for groundwater purification.

Carbon black (CB) NPs have identical optical properties with other carbon-based materials. At longer wavelengths (>1000 nm), their extinction values are even larger than the Au nanocrystal mixtures containing AuNRs with nine different sizes.¹¹⁹ More importantly, they are cheap and widely available, which is beneficial for large-scale solar-thermal applications. In recent years, researchers have started to use CB NPs as solar absorbers in solar distillation. They are usually integrated with a substrate in order to acquire the abilities of self-floating, ease of recycling, and self-cleaning during solar evaporation.¹²⁰ Zhu *et al.* fabricated a flexible Janus absorber by sequential electrospinning of hydrophilic polyacrylonitrile (PAN) and hydrophobic polymethylmethacrylate (PMMA) to form a bilayer membrane, and coating CB NPs on PMMA *via* spray deposition (Fig. 9a).¹²¹ The upper hydrophobic layer composed of CB NPs and PMMA absorbed solar light, while the bottom hydrophilic PAN layer continuously pumped

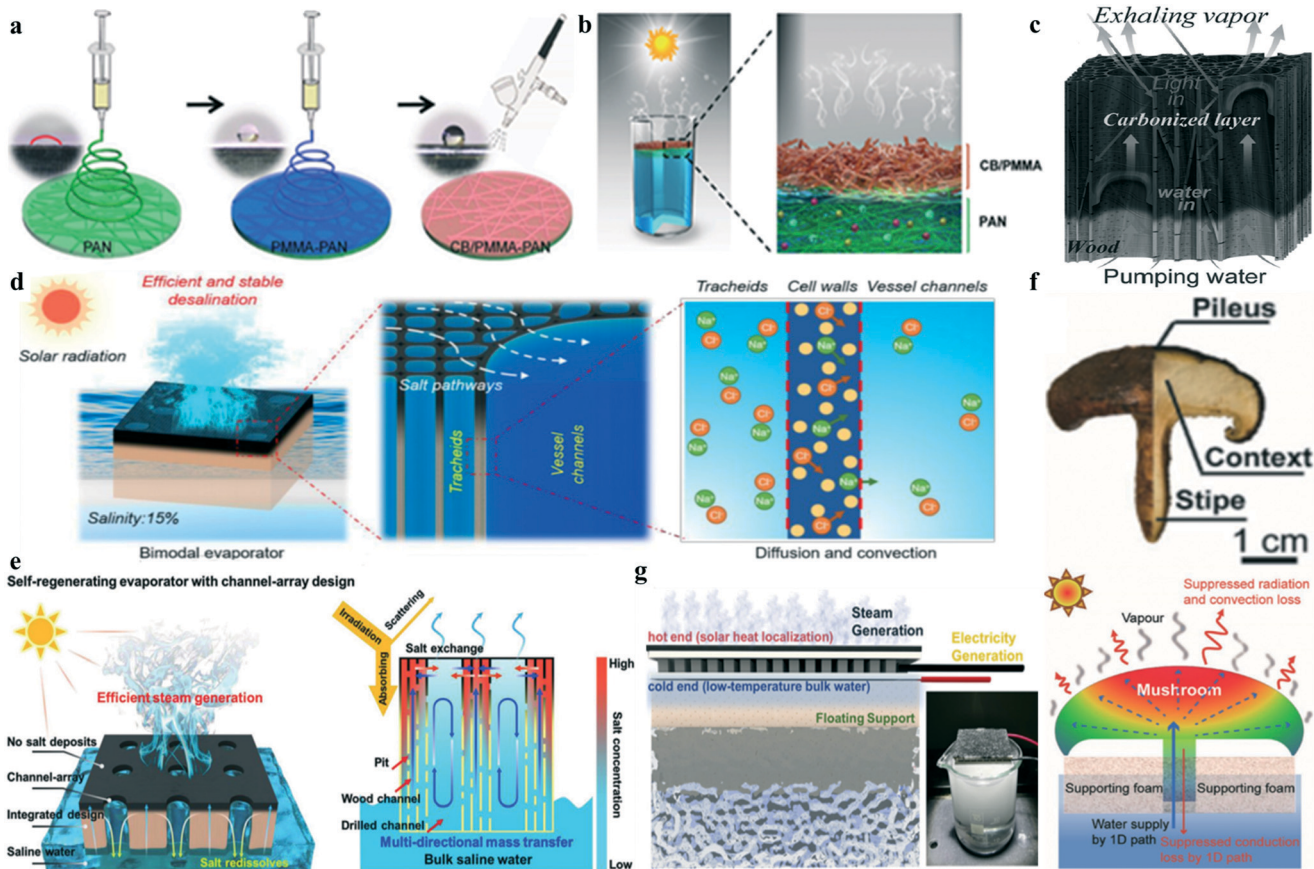


Fig. 9 (a) Fabrication process of the Janus absorber by sequential electrospinning of PAN and PMMA and spray deposition of CB NPs. (b) Schematic structure of the Janus evaporation system in the process of solar desalination. Reprinted with permission from ref. 121 Copyright 2018, Wiley. (c) Solar steam generation based on a bilayer wood structure with the top carbonized portion as the 3D light absorber layer and the bottom hydrophilic natural wood for continuous water transport. Reprinted with permission from ref. 124 Copyright 2017, Wiley. (d) Schematic diagram of the anti-salt accumulation mechanism of the bimodal porous balsa wood-derived evaporator for high salinity brine desalination. Reprinted with permission from ref. 122 Copyright 2019, Royal Society of Chemistry. (e) Schematic illustration of the self-regenerating solar evaporator setup and the working principle of salt rejection via multidirectional mass transfer. Reprinted with permission from ref. 123 Copyright 2019, Wiley. (f) Photo of a shiitake mushroom and schematics of the heat distribution in the mushroom-based evaporator. Reprinted with permission from ref. 126 Copyright 2017, Wiley. (g) Demonstration of the electricity generation process during steam generation. Reprinted with permission from ref. 128 Copyright 2019, Elsevier BV.

water to the top, during which the deposited salts could be rapidly dissolved (Fig. 9b). Thus, the Janus absorber maintained an efficient (72%) and stable water production ($1.3 \text{ kg m}^{-2} \text{ h}^{-1}$, over 16 days) with a photothermal conversion efficiency of 51% under one sun.

Apart from the above-mentioned carbon-based materials, organic substances, including melamine foam (MF) and naturally existed biomass (e.g., wood),^{122,123} can be thermally converted to photothermal carbonaceous materials by carbonization. These carbonized materials not only retain their original internal porous structure, but also have broadband light absorption because of their deep black color and the introduction of conjugated π electrons. The high carbonization degree induced by high pyrolysis temperature can close the energy gaps between the loosely bonded π electrons, facilitating efficient and broadband solar absorption.³³

Taking advantage of the wood's intrinsic features like low thermal conductivity and natural transpiration channels, Hu

et al. designed a series of solar stills using carbonized woods as solar absorber materials.^{122,123} After cutting the natural tree perpendicular to the growth direction, the wood surfaces were carbonized to establish seamless bilayer structures (Fig. 9c).¹²⁴ The upper carbonized layer showed high solar absorption (96–99%), while the lower natural wood layer functioned as microchannels to rapidly pump water upward *via* the capillary effect.^{122,125} To avoid salt accumulation, they either used balsa wood with intrinsic bimodal porous and interconnected microstructures (Fig. 9d), or drilled channel along the growth direction of basswood to construct a hole-array structure (Fig. 9e). The particular channel design enabled the spontaneous interchannel salt exchange between the low salinity region (macro-sized channels) and the high salinity region (micro-sized channels) due to their different hydraulic conductivities, while allowing efficient salt exchange with the subjacent bulk brine to prevent salt accumulation. As a result, highly efficient and long-term

stable evaporation was achieved even for high-salinity solutions (up to 20 wt% NaCl).¹²³

In addition to natural woods, other types of biomass, such as mushrooms,¹²⁶ rice straw,¹²⁷ food wastes,¹²⁸ and natural rape pollens,¹²⁹ have also been carbonized and used as solar absorbers. Among them, carbonized mushrooms have unique structures, with umbrella-shaped black fungus, porous context, and fibrous stipe, which are in favor of effective solar absorption, minimized heat loss, continuous water supply, and accelerated steam escape (Fig. 9f).¹²⁶ Based on the idea of turning “waste” into “treasure”, Tan *et al.* collected several food wastes (FW) like cooked rice and pasta, raw potato, lotus root, and banana peel, to prepare FW-based solar evaporators by carbonization.¹²⁸ The FW-based evaporators were capable of electricity generation during evaporation by exploiting the temperature difference (8 °C) between the hot upper surface and the cold water underneath (Fig. 9g). Interestingly, many special carbon-based materials, such as traditional Chinese ink, cuttlefish juice, and melanin NPs, have also been applied as solar absorbers for water evaporation.

Interestingly, many particular carbon-based materials have also been applied for photothermal conversion in solar desalination. For instance, traditional Chinese ink is an excellent photothermal material.^{130,131} It showed higher photothermal conversion capability and better dispersion stability than Cu and CuO in the nanofluid form.¹³¹ In order to tightly integrate the ink coating with the substrate, Darling *et al.* chose TiO₂ as “glue” to thoroughly cover the Chinese-ink-coated membrane by atom layer deposition.¹³² Carbon NPs like amorphous carbon and graphite were proved to be the main ingredients of Chinese ink by electron energy-loss spectra, which contributed to the broadband light absorption. Similar to Chinese ink, cuttlefish juice is also a good solar absorber due to the dominant ingredient of melanin NPs.¹³³ An evaporation efficiency of 85.8% was achieved by using the extracted melanin NPs as solar absorbers. In addition, the melanin NPs were highly biocompatible, making them promising candidates for safe solar-driven water purification.

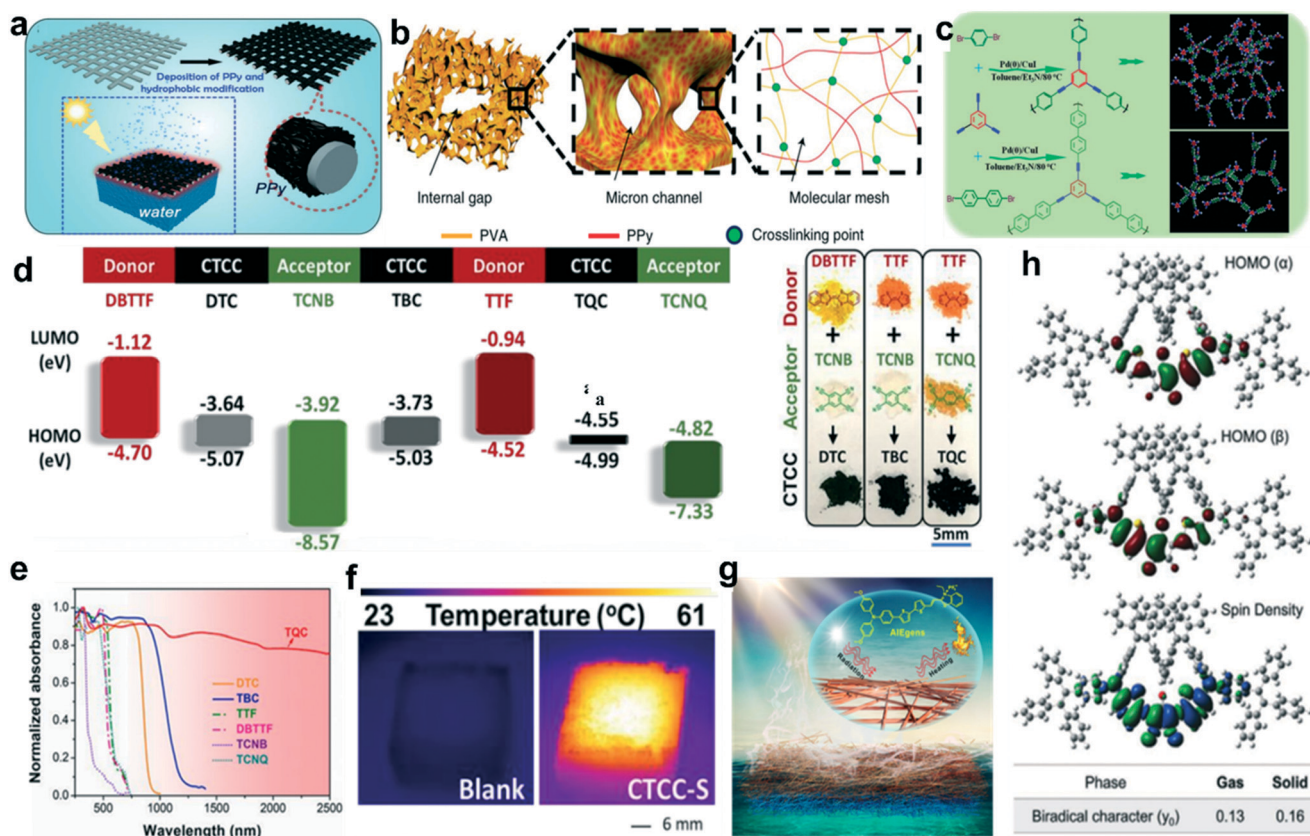


Fig. 10 (a) Schematic diagram of PPy-coated SS mesh for interfacial solar evaporation. Reprinted with permission from ref. 142 Copyright 2015, Wiley. (b) Schematic diagram of the penetration of PPy in the polymeric PVA gel network with hierarchical porous structures (HNG). Reprinted with permission from ref. 145 Copyright 2018, Nature Publishing Group. (c) Synthetic approach of CMP aerogels. Reprinted with permission from ref. 159 Copyright 2018, Royal Society of Chemistry. (d) Calculated energy chart and compositions of CTCCs. (e) Absorption spectra of CTCCs and the corresponding donors and acceptors. (f) Thermographic images of the scaffolds with and without CTCC after illumination under one sun for 3 minutes. Reprinted with permission from ref. 162 Copyright 2020, American Chemical Society. (g) Schematic diagram of 3D AFA doped with photothermal AIE molecules for solar evaporation. Reprinted with permission from ref. 163 Copyright 2020, American Chemical Society. (h) Density functional theory (DFT) calculations of HOMO profiles of the α and β spins and biradical property of CR-TPE-T. Reprinted with permission from ref. 164 Copyright 2020, Wiley.

3.2.2 Conjugated polymers. Conjugated polymers are usually composed of highly π -conjugated polymeric backbones bearing contiguous sp^2 -hybridized carbon atoms like aromatic or heterocyclic rings. Among them, polydopamine (PDA), polypyrrole (PPy), polyaniline (PANI), and conjugated microporous polymers (CMPs) possess outstanding NIR light absorption and photothermal conversion properties and have been recently used as solar absorbers for water evaporation.

PDA stands out among large amounts of conjugated polymers due to its merits, including universal adhesion, high chemical activity, and good biocompatibility. It is formed by spontaneous oxidation of dopamine, intramolecular cyclization, and oligomerization or aggregation.^{134,135} In recent years, PDA has been used as a photothermal coating material for a variety of porous materials with low thermal conductivity, for instance, wood ($0.13 \text{ W m}^{-1} \text{ K}^{-1}$),¹³⁶ bacterial nanocellulose (BNC) ($0.024 \text{ W m}^{-1} \text{ K}^{-1}$),¹³⁷ cotton ($0.04 \text{ W m}^{-1} \text{ K}^{-1}$),¹³⁸ and sponge ($0.29 \text{ W m}^{-1} \text{ K}^{-1}$),¹³⁹ to construct PDA-based evaporators. By adjusting the size of PDA particles, the optical absorption could be optimized to maximally match the solar spectrum.¹³⁷

PPy is also a potential solar absorber due to its high photothermal conversion efficiency, low thermal conductivity, and facile fabrication process.^{140,141} Wang *et al.* reported for the first time a PPy-based evaporator with hydrophobic self-healing capability.¹⁴² The stainless steel (SS) mesh was coated with PPy, which was further modified with a fluoroalkyl silane moiety to introduce self-healing hydrophobicity (Fig. 10a). However, heat loss was unavoidable because of the high thermal conductivity of the metal scaffold. Thus, Yu's group made use of polymeric hydrogels to eliminate the convective heat loss.^{143,144} In general, PPy was penetrated into the polyvinyl alcohol (PVA) gel network containing internal gaps, micron channels, and molecular meshes (Fig. 10b),¹⁴⁵ allowing direct heat transfer to the trace water confined in the molecular meshes in the process of solar vapor generation. Therefore, the hydrogel-based evaporators showed extremely high water evaporation rates ($>3.2 \text{ kg m}^{-2} \text{ h}^{-1}$) and solar steam generation efficiency ($>92\%$). Inspiringly, PPy can be used as a universal coating on the surface of various substrates, such as cellulose paper,¹⁴⁶ polyamide nanofibers,¹⁴⁷ air-laid paper,¹⁴⁸ commercial melamine sponge,¹⁴⁹ maize straw,¹⁵⁰ black sand,¹⁵¹ and natural latex foam.¹⁵²

Recently, PANI and CMPs have been used as solar absorbers.¹⁵³ Yang *et al.* innovatively constructed a double-crosslinked PANI-based hydrogel, which showed a maximum photothermal efficiency of 91.5% and an evaporation rate of $1.40 \text{ kg m}^{-2} \text{ h}^{-1}$.¹⁵⁴ Owing to the flexible functional groups, shape, and size of CMPs, it is feasible to systematically regulate the π -coupling porous structure, thereby optimizing the framework for desirable performance in adsorption, catalysis, and photothermal conversion.¹⁵⁵ In addition, CMPs have high hydrophobicity,¹⁵⁶ efficient light absorption, and low thermal conductivity.^{157,158} In 2018, Li's group firstly

designed highly porous CMP aerogels for solar evaporation.^{159,160} The 3D architectures were constructed from CMP nanotubes synthesized by the Sonogashira-Hagihara cross-coupling reaction between 1,3,5-triethynylbenzene and 1,4-dibromobenzene or 4,4'-dibromobiphenyl (Fig. 10c). The evaporation rates of CMP aerogels were relatively low ($<1.0 \text{ kg m}^{-2} \text{ h}^{-1}$), which could be increased to 1.3992 and $1.4406 \text{ kg m}^{-2} \text{ h}^{-1}$, respectively, by coating with a carbon black layer or carbonizing the CMP aerogels. However, these π -conjugated polymers will inevitably undergo aging and decomposition under long-term sunlight exposure due to the intrinsic organic features, shortening the service life.¹⁶¹ How to effectively improve the stability and broaden the optical absorption of these materials is worthwhile to explore in the future study.

3.2.3 Small-molecule organic solar absorbers. Organic small molecules possess some intrinsic advantages such as flexibility, structure diversity, and tunable properties. However, their low solar-thermal conversion efficiency induced by the narrow absorption band limits their application in solar evaporation. To solve this problem, Lee *et al.* prepared charge transfer complex co-crystals (CTCCs) by combining different donor and acceptor small molecules, which showed broadband absorption due to the small energy gaps (Fig. 10d).¹⁶² The CTCC formed between tetrathiafulvalene (TTF, donor) and tetracyanoquinodimethane (TCNQ, acceptor) showed full solar spectrum absorption and excellent photothermal performance (Fig. 10e and f). For the first time, the CTCC was applied as a solar absorber by being loaded on the 3D porous polymer scaffold, achieving an evaporation rate of $1.67 \text{ kg m}^{-2} \text{ h}^{-1}$ and a solar conversion efficiency of 90.3%. Another approach to broaden the light absorption was to dope aggregation-induced emission (AIE) photothermal molecules into a 3D all-fiber aerogel (AFA) (Fig. 10g).¹⁶³ Owing to the extended optical length and attenuated reflection induced by the AFA's interconnected porous structure, broadband absorption from 200 to 2500 nm was achieved, enabling highly efficient solar evaporation. Meanwhile, the same group designed a croconium derivative (CR-TPE-T) with the absorption range covering 300–1600 nm due to the features of unique biradical property and strong π – π stacking (Fig. 10h).¹⁶⁴

3.3 Electron-hole generation and relaxation

The photothermal conversion of inorganic semiconductors is based on the generation of free carrier in the bandgap.¹⁷⁰ When the incident light energy is higher than the bandgap energy, the above-bandgap electron-hole pairs are generated.^{33,171} Before recombining, the electrons and holes relax to the edges of the conduction band (CB) and valence band (VB), converting the excess energy into heat *via* non-radiative relaxation. In contrast, the recombination of electron-hole pairs near the bandgap edge is accompanied with energy release *via* photoluminescence (radiant recombination), which is adverse to heat generation (Fig. 11a and b).^{28,172} Therefore, in order to enhance the

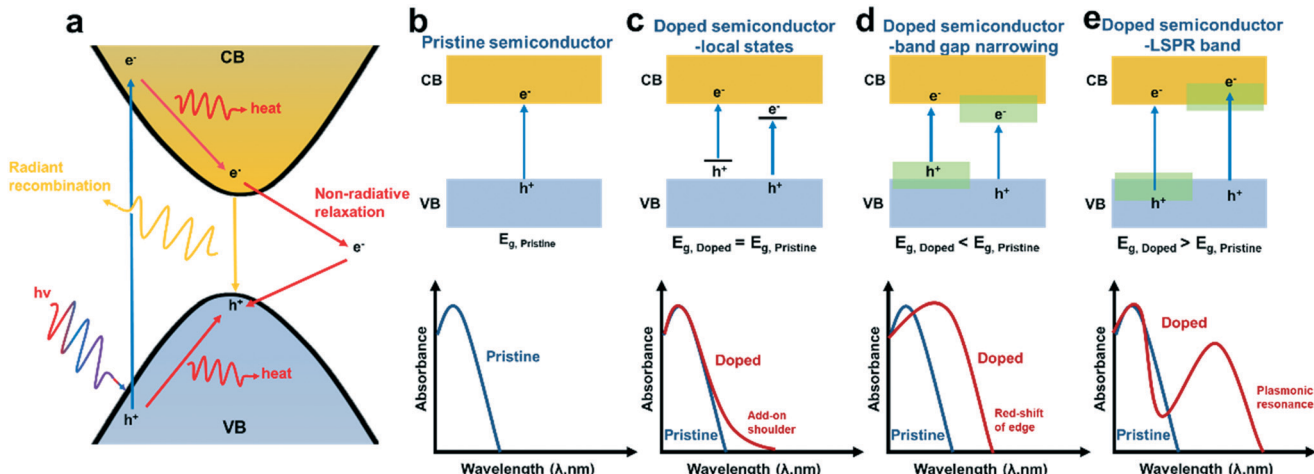


Fig. 11 (a) Photothermal conversion mechanism via non-radiative relaxation of semiconductors. The band structure and optical absorption curves of the pristine semiconductor (b) and doped semiconductors with intraband energy states (c), a narrowed band gap (d), and an introduced LSPR band (e).

photothermal efficiency, it is important to improve the optical absorption in the vis-NIR regions by manipulating the electronic band structure.^{13,106} In general, doping is commonly used to extend the light absorption of semiconductors through introducing the intraband energy states (Fig. 11c), narrowing the bandgap (Fig. 11d), and creating the LSPR band (Fig. 11e). The introduced intraband energy states show an add-on shoulder on the edge of the absorbance spectrum (Fig. 11c). In addition, the narrower band gap not only makes the entire light absorption edge move towards the longer wavelength, but also facilitates the photocatalytic process (Fig. 11d). Moreover, the newly emerged LSPR band is mainly distributed in the NIR region (Fig. 11e) (see 3.1.4 Plasmonic semiconductor). The detailed mechanisms have been elaborated in previous reviews.^{173,174} In this section, we summed up the application of photothermal semiconductors in solar evaporation (Table 3).

3.3.1 Metal oxides. Titanium dioxide (TiO_2) NPs are widely used in photocatalysis.¹⁷⁵ However, the optical absorption is always limited to <400 nm due to their intrinsic large bandgap (3.0–3.2 eV).¹⁷⁶ Therefore, researchers have devoted a lot of effort to narrow their bandgap in order to make the utmost use of solar light. As a milestone, the first black titania with black color and a bandgap of 1.5 eV was prepared by Mao's group in 2011.¹⁷⁵ Although the light absorption has been extended to 800 nm, only 40% of the entire solar energy can be utilized.

In order to widen the light absorption to the full solar spectrum range for efficient solar–thermal conversion, the bandgap of TiO_2 should be further decreased. For this purpose, Wu *et al.* produced nanosized titanium sesquioxide (Ti_2O_3) with an extremely small band gap (~0.1 eV) from commercial Ti_2O_3 powders by ball milling.¹⁷⁷ Due to enhanced light scattering, the light absorption ability of nanosized Ti_2O_3 was greatly improved. The Ti_2O_3 NPs can absorb 92.5% of the full solar spectrum with an external

solar–heat conversion efficiency of 92.1%, indicating a nearly 100% internal conversion efficiency. Soon after, Ozin *et al.* synthesized black TiO_x NPs by reducing white P25 TiO_2 nanocrystals with magnesium (Mg).¹⁷⁸ As the amount of Mg increased, the color of TiO_x NPs was gradually darkened, accompanied by the decreased x values and enhanced light absorption. The black TiO_x had the highest solar absorption (91.3%), which was spin-coated on the surface of the stainless steel mesh, and then subjected to fluoroalkylation for superhydrophobization. The photothermal conversion efficiency reached 50.3% under one sun. Later on, Huang *et al.* synthesized black titania with a unique nanocage nanostructure, which enhanced the efficiency to 70.9% (Fig. 12a).¹⁷⁹ In view of the difficulty of the solar evaporation technique in the treatment of volatile-organic-compounds (VOCs) containing a water source, Wang's group fabricated a mesoporous oxygen vacancy-rich TiO_{2-x} nanofibrous membrane (m- TiO_{2-x} NFM) by the combination of electrospinning, sol-gel coating, and magnesiothermic reduction for intercepting and *in situ* degrading VOCs during solar evaporation (Fig. 12b).¹⁸⁰ Under solar irradiation, m- TiO_{2-x} NFM exhibited excellent photothermal and photocatalytic activities simultaneously due to the existence of a broad mid-bandgap offered by oxygen vacancies, allowing light-driven photocatalytic VOC interception in the process of solar evaporation (Fig. 12c).

Different from most Cu-based solar absorbers that undergo the LSPR-induced photothermal effect, copper oxide (CuO) and copper phosphate can generate heat *via* non-radiative relaxation.^{181,182} Inspired by the water transportation process of natural trees, Wang *et al.* designed a CuO tree solar evaporation system, which possessed abundant CuO nanowires on a copper mesh. The CuO tree system could degrade pollutants by combining the photocatalytic degradation of the upper CuO layer under solar light and the activation of potassium monopersulfate of

Table 3 Properties, parameters, and performance of semiconductor material-based solar evaporators

| Solar absorbers | Power density (kW m^{-2}) | Wavelength range (nm) | Absorption (%) | Solar-thermal efficiency (%) | Solar-steam efficiency (%) | Evaporation rate ($\text{kg m}^{-2} \text{ h}^{-1}$) | Thermal conductivity ($\text{W m}^{-1} \text{ K}^{-1}$) | Stability/scalability | Surface property | Ref. |
|------------------------------------|--------------------------------------|-----------------------|----------------|------------------------------|----------------------------|--|---|-----------------------|------------------|------|
| Ti ₂ O ₃ NPs | 1 | 250–2500 | 92.5% | — | — | 1.32 | 0.02 | 25 cycles | Hydrophilic | 177 |
| CuO nanowires | 1 | 200–2500 | 93.8 | — | 84.4 | 1.42 | 0.02 | Stable | Hydrophilic | 212 |
| HN/NiO | 1 | 250–2500 | 92.1 | — | 85.8 | 1.38 | — | Stable | Hydrophilic | 184 |
| 2H-DMM-SA | 1 | 250–2500 | 80–90 | — | 83.8 | 1.68 | — | 72 h scalable | Hydrophilic | 213 |
| 3D MoS ₂ aerogel | 1 | 200–2500 | 95 | — | 88 | 1.27 | 0.37 | Stable | Hydrophilic | 194 |
| BSSG | 1 | 300–2500 | ~90 | — | 84.1 | 1.28 | 0.44 | Stable | Hydrophilic | 203 |
| SiO ₂ /BP-MT | 1 | 300–2500 | ~75 | — | 74 | 1.63 | — | 10 days | Hydrophilic | 209 |
| MHS | 1 | 250–2500 | 97.6 | — | 96 | 1.5 | — | Stable | Hydrophilic | 210 |
| HHE | 1 | 400–2500 | 98 | — | 90 | 3.2 | 0.25–1.08 | Scalable | — | 211 |

the bottom part for oxidation decontamination in the dark (Fig. 12d).

Moreover, by introducing defects and an intermediate energy level to nickel oxide (NiO), black NiO was generated with a narrowed bandgap, which has been used in photocatalysis due to the broadband absorption.¹⁸³ The potential application of black NiO as a photothermal material for solar evaporation was explored by Xiong and his colleagues.¹⁸⁴ Black NiO NPs were deposited on the substrate made of hydroxyapatite nanowires and glass fibers to generate the HN/NiO solar evaporator (Fig. 12e). The HN/NiO photothermal film had an absorption efficiency of 92.1% in the full solar spectrum, owing to the inherent optical absorption characteristics of black NiO NPs and extended light path originating from the porous structure of the black NiO layer.

3.3.2 Transition metal chalcogenides (TMCs). As a representative 2D TMC, molybdenum disulfide (MoS₂) exhibits excellent absorption in the vis-NIR range. Surprisingly, the light absorption of monolayer MoS₂ (5–10% of incident sunlight) is better than graphene (2.3%), and even 10 fold stronger than the most widely used solar absorber in solar cells, such as GaAs and Si.^{185,186} Moreover, the narrow bandgap (1.2–1.9 eV) allows for heat generation *via* non-radiative decay of the electron-hole pairs.¹⁸⁷ MoS₂ has been used as a photothermal agent for cancer therapy,¹⁸⁸ imaging,¹⁸⁹ antibacterial application,¹⁹⁰ and solar-assisted crude oil recovery.^{191,192} Jun *et al.* extended the application of MoS₂ to solar distillation.¹⁹³ Chemically exfoliated MoS₂ (ce-MoS₂) was fabricated by Li-intercalation, during which the phase transition from 2H to 1T occurred, leading to the enhancement of light absorption due to the narrower bandgap of 1T-phase MoS₂. Using bacterial nanocellulose (BNC) as a polymer matrix with hydrophilic property and low thermal conductivity, a solar evaporator based on ce-MoS₂/BNC was fabricated (Fig. 12f). The solar evaporation efficiency of ce-MoS₂/BNC was 6.15 kg m⁻² h⁻¹, which was much higher than that of bulk MoS₂/BNC (4.73 kg m⁻² h⁻¹) under 5.35 kW m⁻². Wang *et al.*¹⁹⁴ prepared a three-dimensional MoS₂ aerogel, which has a light absorption efficiency of >95% in the entire solar spectrum, and its evaporation rate can reach >90% under a sunlight of 1.5–3.0 kW m⁻². In addition, many other MoS₂-based solar evaporation systems, such as the MoS₂ nanoflower-based solar evaporator,¹⁹⁵ double-layer MoS₂@sponge,¹⁹⁶ and PEGylated MoS₂-cotton cloth,¹⁹⁷ have been developed for water evaporation, as well as wastewater treatment.

Compared to binary TMCs (*e.g.*, MoS₂), ternary TMCs, such as CuFeS₂ and CuFeSe₂, are more flexible in functional regulations and applications.^{198,199} For example, Hu's team loaded narrow-bandgap CuFeSe₂ NPs on a piece of wood for desalination.²⁰⁰ The narrow bandgap of CuFeSe₂ NPs (0.45 eV) ensured full spectrum solar absorption and efficient heat generation,²⁰¹ since most photons activated by sunlight have much higher energy than the bandgap. The CuFeSe₂ NP-decorated wood membrane has a solar thermal efficiency of

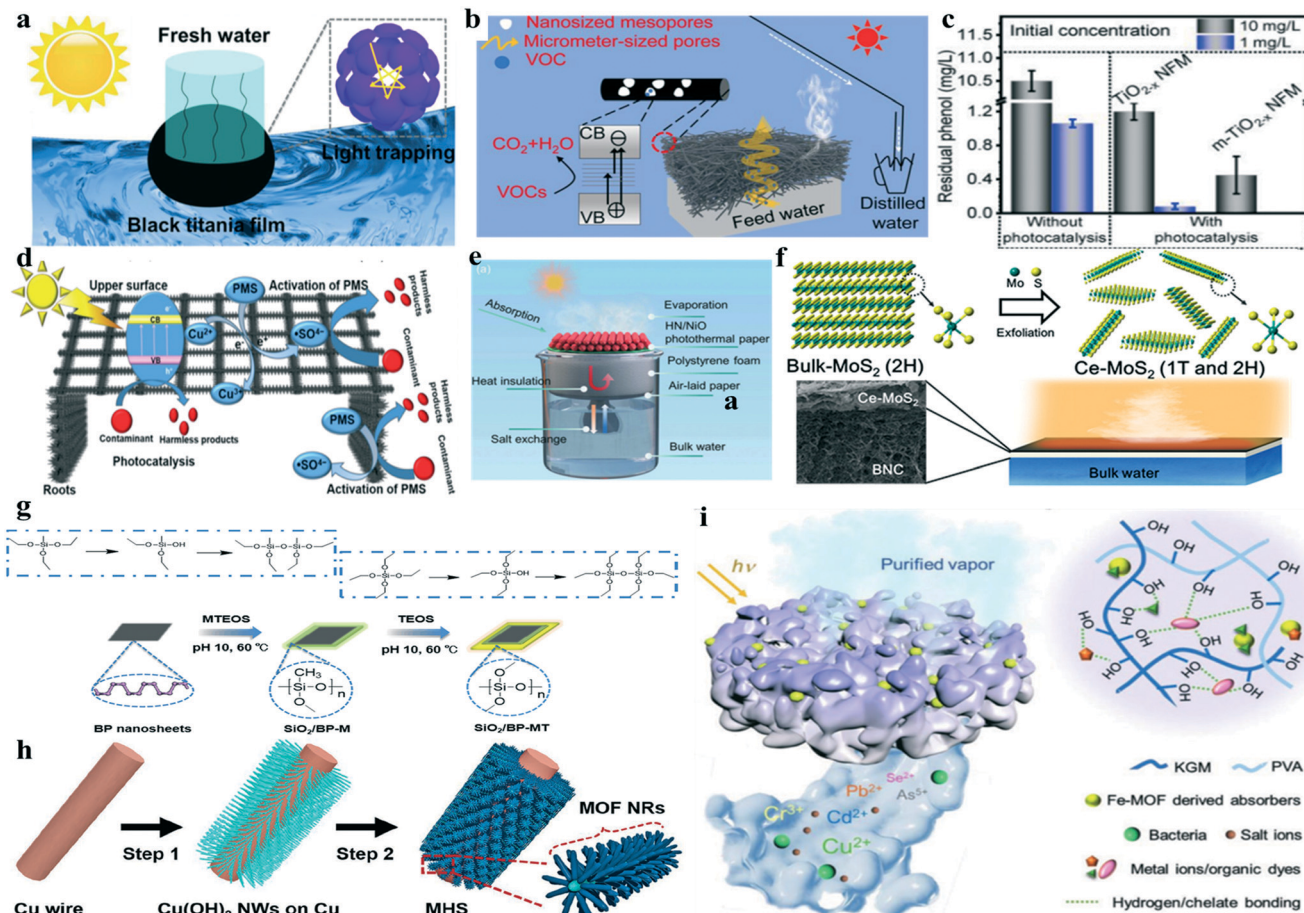


Fig. 12 (a) Schematic diagram of the black titania nanocage film-based solar desalination. Reprinted with permission from ref. 179 Copyright 2016, American Chemical Society. (b) Schematic diagram of the m-TiO_{2-x} NFM-based evaporator for *in situ* VOC interception during solar distillation. (c) Performance of VOC interception under different conditions. Reprinted with permission from ref. 180 Copyright 2020, American Chemical Society. (d) Schematic diagram of pollutant degradation during solar evaporation based on the CuO nanowire mesh. Reprinted with permission from ref. 212 Copyright 2019, American Chemical Society. (e) Schematic diagram of the construction of the HN/NiO solar evaporator. Reprinted with permission from ref. 184 Copyright 2020, Royal Society of Chemistry. (f) Preparation processes of ce-MoS₂/BNC. Reprinted with permission from ref. 193 Copyright 2018, Elsevier BV. (g) Preparation processes of silica-coated BP nanosheets. Reprinted with permission from ref. 209 Copyright 2020, Royal Society of Chemistry. (h) Preparation processes of MHS. Reprinted with permission from ref. 210 Copyright 2019, Wiley. (i) Schematic diagram of solar distillation-based water purification by HHEs. Reprinted with permission from ref. 211 Copyright 2020, Wiley.

86.2% under 5 kW m⁻² and a solar light absorption of 99% in the full spectral range.

In addition to the direct bandgap of TMCs, indirect-bandgap TMCs like SnSe and SnSe₂ also have high photothermal conversion capacity due to the efficient phonon generation and low thermal conductivity.²⁰² However, the limited light absorption in the full solar spectrum impedes their application in solar evaporation. To solve this issue, Jang *et al.* deposited a large-area SnSe-SnSe₂ layer on a glassy carbon form (CF) by the pulsed laser deposition (PLD) technique to construct a bilayer solar steam generator (BSSG).²⁰³ This system possessed broadband solar absorption due to the trap of incident light in the porous CF, which induced maximized light absorption. Therefore, an evaporation efficiency as high as 84.1% was achieved under one sun.

3.3.3 Black phosphorus (BP). BP nanosheets are newly emerging 2D semiconductors with a thickness-dependent

direct bandgap (0.3–2.0 eV). The narrow bandgap of BP nanosheets accounts for their broadband absorption in the vis-NIR spectral range.²⁰⁴ In addition, BP nanosheets show higher photothermal conversion efficiency at 808 nm than the commonly used photothermal agents, such as AuNPs, Ti₂C₃ nanosheets, and TMCs.^{205,206} On this basis, Hu *et al.* deposited negatively charged BP nanosheets and positively charged chitosan (CS) on the scaffold of polyurethane (PU) foam by electrostatic layer-by-layer assembly to form a BP nanosheet-based solar steam generator.²⁰⁷ An evaporation rate of 1.082 kg m⁻² h⁻¹ was achieved under one sun. However, BP nanosheets are liable to degradation in the presence of oxygen and water, which hinders the long-term stability during solar evaporation.²⁰⁸ To improve the aqueous stability, our group coated a layer of hydrophobic silica shell on the surface of BP nanosheets by hydrolytic condensation of siloxane.²⁰⁹ After that, a second hydrophilic silica shell

was formed on the outer surface to obtain the double-layered silica-coated BP nanosheets ($\text{SiO}_2/\text{BP-MT}$), which showed obvious improvement in aqueous stability (Fig. 12g). The evaporator based on the $\text{SiO}_2/\text{BP-MT}$ film had a solar evaporation rate of $1.63 \text{ kg m}^{-2} \text{ h}^{-1}$ under one sun and the evaporation rate was stable for at least 10 days, demonstrating that passivation with a hydrophobic silica shell is an effective approach for life-extending of BP nanosheets in the application of solar evaporation.

3.3.4 Metal organic frameworks (MOFs). MOFs have received extensive attention in photocatalysis and photothermal catalysis in recent years, although they have not served as photothermal agents in solar evaporation until the first report by Zhang *et al.* in 2019. Taking advantage of the intrinsic broadband absorption of Cu-CAT-1 MOF, they designed a MOF-based hierarchical structure (MHS) for water evaporation (Fig. 12h).²¹⁰ The MHS not only showed efficient absorption (97.6%) in the full spectrum range and a high water evaporation rate ($1.50 \text{ kg m}^{-2} \text{ h}^{-1}$), but also has good anti-oil-fouling performance, rendering it an excellent solar evaporator even in oil-contaminated water. Very recently, Yu *et al.* introduced photothermal NPs derived from an iron-based MOF and a naturally abundant biomass, konjac glucomannan (KGM), into polyvinyl alcohol (PVA) networks to construct a hybrid hydrogel evaporator (HHE) with low cost ($\$14.9 \text{ m}^{-2}$ of total materials cost) and a high evaporation rate ($3.2 \text{ kg m}^{-2} \text{ h}^{-1}$ under one sun) against various wastewaters and concentrated seawater.²¹¹ In HHE, KGM contributed to water activation by increasing the hydrogel's hydration ability, while both KGM and MOF were responsible for the high adsorption capacity to contaminants (Fig. 12i). This study offers an opportunity to balance the efficiency and cost during the promotion of practical solar desalination.

3.4 Hybrid solar absorbers

A single photothermal material often has limitations in one or several of the criteria for ideal solar absorbers. Lately, attention has been paid to combining different types of photothermal agents for the enhancement of solar light harvesting capacity, photothermal conversion capacity, and long-term stability.²¹⁴ In this section, we presented some combinations of solar absorbers that can draw on each

other's strength for the enhanced performance of the photothermal effect (Table 4).

3.4.1 Hybridization of plasmonic materials. Integration of plasmonic materials with different plasmon resonance regions has been conducted to enhance the optical absorption in photocatalytic degradation,²¹⁵ cancer therapy,²¹⁶ hydrogen evolution reaction,²¹⁷ and solar evaporation in a recent study.²¹⁸ Inspired by the enhanced photothermal performance of Au–CuS yolk-shell NPs due to the LSPR coupling between Au and CuS, Zhang *et al.* fabricated Au–CuS gyroid-structured materials (Au–CuS/GMs) by a sol-gel technique for high-performance solar evaporation.²¹⁸ Upon irradiation, electron transfer occurred from CuS to Au, since SPR of Au and CuS derived from the collective oscillations of electrons and holes, respectively. Hence, the light absorption was enhanced due to the increased SPR performance of the Au–CuS hybrid. Apart from LSPR coupling, the 3D helices enabled antireflection *via* a large scattering cross-section, which further enhanced the solar absorption. As a result, a high evaporation efficiency of 88.8% was obtained with an extremely low loading content of the photothermal material ($<1 \text{ mg cm}^{-2}$).

3.4.2 Hybridization of plasmonic and carbonaceous materials. Carbonaceous materials always act as substrates for plasmonic NPs to improve the photothermal performance and mechanical stability. For instance, a bilayer Janus film was formed by assembling AuNR on the CNT-based porous film (Fig. 13a),²¹⁹ which has efficient optical absorption (98%) in the wavelength range of 300–2500 nm. The high absorption originated from both materials, as well as the increased optical path length induced by the strong light scattering of nanosized AuNRs. Similarly, other carbonaceous materials, including rGO, N-doped rGO, and carbonized organosilica (c-silica) microspheres, have also been hybridized with AuNPs, allowing for the synergistic photothermal effects.^{220,221} In addition to AuNPs, other plasmonic materials, such as Cu and Ag, have also been composited with carbonaceous materials. Huang *et al.* developed Cu nanodot-embedded N-doped graphene urchins as a highly efficient self-floating solar absorber (Fig. 13b).²²² The plasmonic energy inside Cu nanodots activated by the incident photons was transferred to graphene through direct electron transfer, which allowed for the hybridized LSPR, thus endowing almost full solar absorption (99%) in the spectral range of 300–1800 nm. The functions of the 3D

Table 4 Properties, parameters, and performance of hybrid material-based solar evaporators

| Solar absorbers | Power density (kW m^{-2}) | Wavelength range (nm) | Absorption (%) | Solar-steam efficiency (%) | Evaporation rate ($\text{kg m}^{-2} \text{ h}^{-1}$) | Thermal conductivity ($\text{W m}^{-1} \text{ K}^{-1}$) | Stability/scalability | Surface property | Ref. |
|--|--------------------------------------|-----------------------|----------------|----------------------------|--|---|-----------------------|------------------|------|
| SWNT/AuNR film | 5 | 300–2500 | 98 | 94 | 6.7 | 0.2 | 24 cycles | Hydrophobic | 219 |
| Cu nanodot-embedded N-doped graphene urchins | 1 | 300–1800 | 99 | 82 | 0.63 | — | 10 cycles | Hydrophilic | 222 |
| Ag@PDA NPs | 1 | 280–2500 | 98.65 | 97 | 2.08 | 0.03 | Stable | Hydrophilic | 230 |
| CTF-tertA/CNT | 1 | 250–2000 | 97 | 93.2 | 1.59 | 0.108 | Stable | Hydrophilic | 233 |

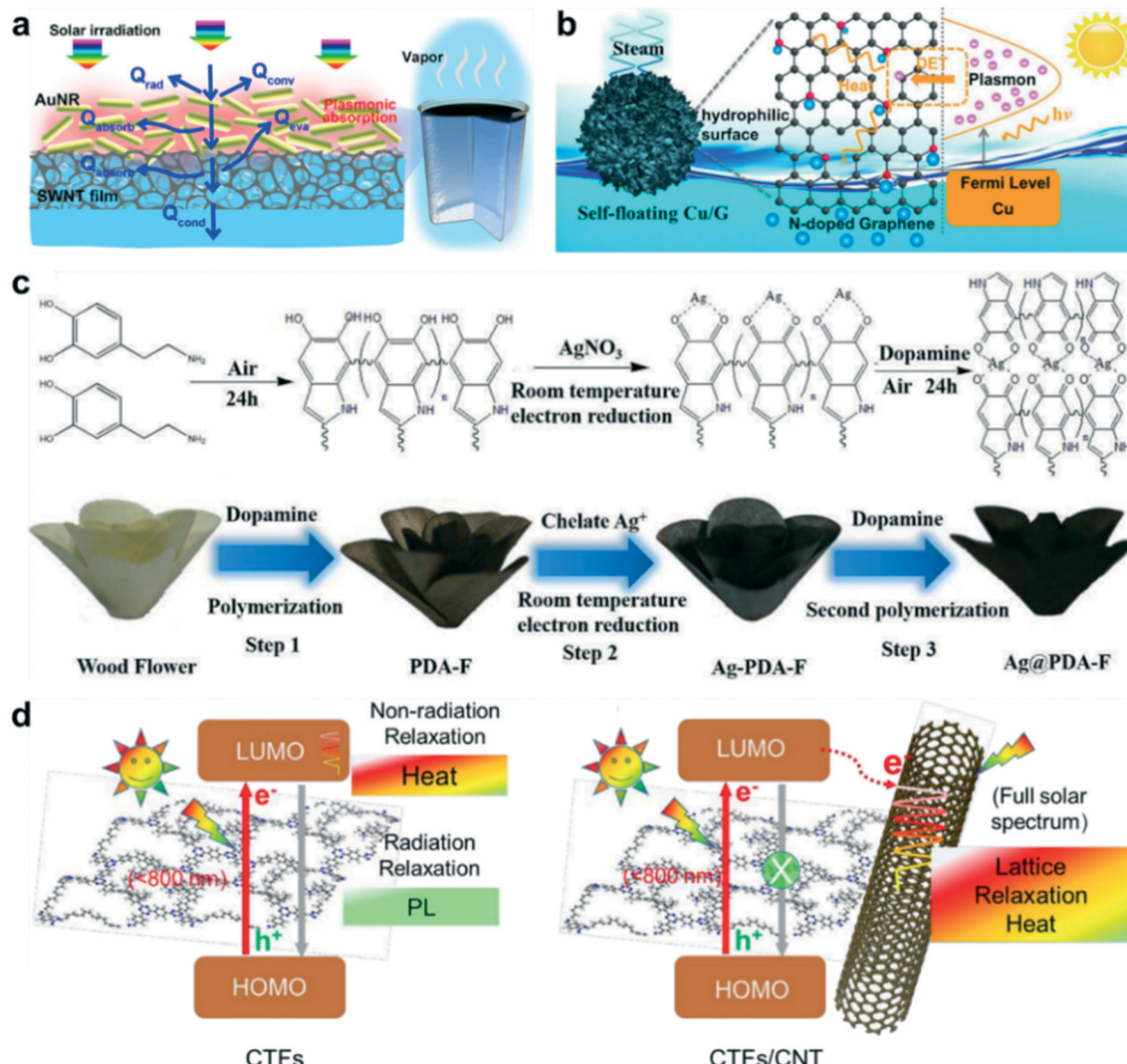


Fig. 13 (a) Schematic of the SWNT/AuNR film-based interfacial evaporation system. Reprinted with permission from ref. 219 Copyright 2018, American Chemical Society. (b) Schematic of plasmon-enhanced solar desalination of Cu nanodot-embedded N-doped graphene urchins via direct electron transfer. Reprinted with permission from ref. 222 Copyright 2018, Elsevier BV. (c) Fabrication process of the plasmonic wooden flower. Reprinted with permission from ref. 230 Copyright 2018, Elsevier BV. (d) Schematic illustration of the charge migration and heat generation process in CTFs and CTFs/CNT. Reprinted with permission from ref. 233 Copyright 2020, American Chemical Society.

interconnected graphene matrix included promoting the electron transportation and converting extra energy into heat *via* thermalization, protecting Cu nanodots from oxidation, providing freeway for water transport, and endowing the self-floating property. As a result, stable and efficient desalination was achieved. Similarly, Ag or Ag/Au nanocube-based plasmonic colloidosomes composited with GO were likewise highly efficient in solar-driven water desalination.²²³

3.4.3 Hybridization of plasmonic and semiconductor materials. In order to improve the solar absorption capacity of plasmonic NPs, semiconductors can be introduced to broaden their absorption bandwidth. For example, TiO_2 has been used as a semiconductor coating for plasmonic NPs. It can absorb the UV light of the solar spectrum for photocatalysis without interfering with the absorption of vis-NIR light by the photothermal plasmonic

core (*e.g.*, Au and Ag).^{224,225} In particular, Ho *et al.* prevented the direct contact between AgNPs and the TiO_2 shell by introducing a SiO_2 dielectric spacer, which could protect AgNPs from detrimental oxidation, aggregation, and migration.²²⁶ Apart from serving as a semiconductor shell, TiO_2 could also be hybridized with Al NPs by ball milling to form the Al-Ti-O nanostructure.²²⁷ During the process, TiO_2 was partially reduced by Al NPs, resulting in the conversion of Ti^{4+} to Ti^{3+} accompanied with the formation of oxygen vacancies, which was in favor of light harvesting. Meanwhile, the oxide layer in Al NPs extended the absorption to the IR region due to the alteration of the dielectric environment. As a result, broadband absorption covering 90.32% of the solar spectrum was achieved attributed to the synergistic LSPR effect of Al and high photoactivity of black TiO_2 .

In addition to hybridization with TiO_2 , coating with conjugated polymers has also been used to improve the photothermal effect of plasmonic NPs.²²⁸ When the plasmonic NPs were coated with a polymer shell, the plasmon resonance absorption was red-shifted due to the restriction of electron vibration in a smaller space.²²⁹ On this basis, Liu *et al.* designed Ag@PDA core–shell structured NPs by covering AgNPs with PDA and loaded them on the wooden flower (Fig. 13c).²³⁰ Due to the hybridized LSPR effect of the randomly distributed AgNPs close-packed in PDA layer, the Ag@PDA loaded plasmonic wooden flower showed superior light absorption (98.65%), resulting in efficient vapor generation ($2.08 \text{ kg m}^{-2} \text{ h}^{-1}$) and solar-to-vapor conversion (97%).

3.4.4 Hybridization of carbonaceous and semiconductor materials. The combination of carbonaceous and semiconductor materials can improve the optical absorption to make the utmost of solar light. Hu *et al.* synthesized a 3D macrostructure CuFeSe₂-loaded graphene aerogel.²³¹ Reduced GO (rGO) decreased the electron density of CuFeSe₂, resulting in blueshift in absorbance.²³² Therefore, rGO can extend the absorption spectrum of CuFeSe₂ to longer wavelengths. As discussed earlier in 3.2, radiative emission (fluorescence) is competitive with non-radiative relaxation-induced heat generation in the process of energy release. Therefore, besides improving the light harvesting capacity, suppressing the radiation relaxation is equally important to enhance the photothermal effect. Hence, a high-performance donor–acceptor composed of CNT and a superhydrophilic covalent triazine framework (CTF) was fabricated to mitigate the undesirable radiative relaxation-induced energy loss.²³³ Due to the strong electron trapping capability of CNT, it could capture and store excited electrons in CTFs to delay the charge recombination, so that the energy release of radiation relaxation was suppressed (Fig. 13d). Moreover, CNT can also extend the light absorption range, facilitating an outstanding evaporation performance.

4. Summary and prospects

Thanks to the tremendous progress in the synthesis and innovation of solar absorbers, solar evaporation has regained huge attention as a promising approach to solve the worldwide problem of water shortage. Herein, we overviewed the current achievements of various solar absorption materials used for solar evaporation. On the basis of understanding the photothermal mechanisms of LSPR, thermal vibration of molecules, and electron–hole generation and relaxation, the strategies of advancing solar absorbers were discussed.

The performance of solar evaporators based on each type of solar absorber is systematically and comprehensively summarized and listed in Tables 1–4. To be specific, the evaporation rate of plasmonic material-, carbonaceous material-, and semiconductor material-based evaporators were in the range of 1.008–1.657, 0.92–3.2, and $1.27\text{--}3.2 \text{ kg m}^{-2} \text{ h}^{-1}$, respectively. Although the hybrid material-based evaporators did not show apparent superiority in the evaporation rate ($0.63\text{--}2.08 \text{ kg m}^{-2} \text{ h}^{-1}$), their absorption efficiency (97–99%) and solar-to-steam conversion efficiency (82–97%) were generally higher than those of single solar absorber-based evaporators.

While many solar absorbers possess high absorption efficiencies, each type has its own pros and cons (Fig. 14). For instance, plasmonic absorbers have intensive light absorption and strong photothermal conversion capacities, whereas they are usually chemically unstable, expensive, and difficult to fabricate on a large scale, which are obstacles for their practical applications. In contrast, carbon-based materials, in particular carbonized biomass, are widely available, low cost, scalable, and environmental benign. In spite of this, their stability against water, heat, and bacteria should be concerned. In addition, photothermal polymers have some unique features compared to their inorganic counterparts, such as flexibility, moldability, and water

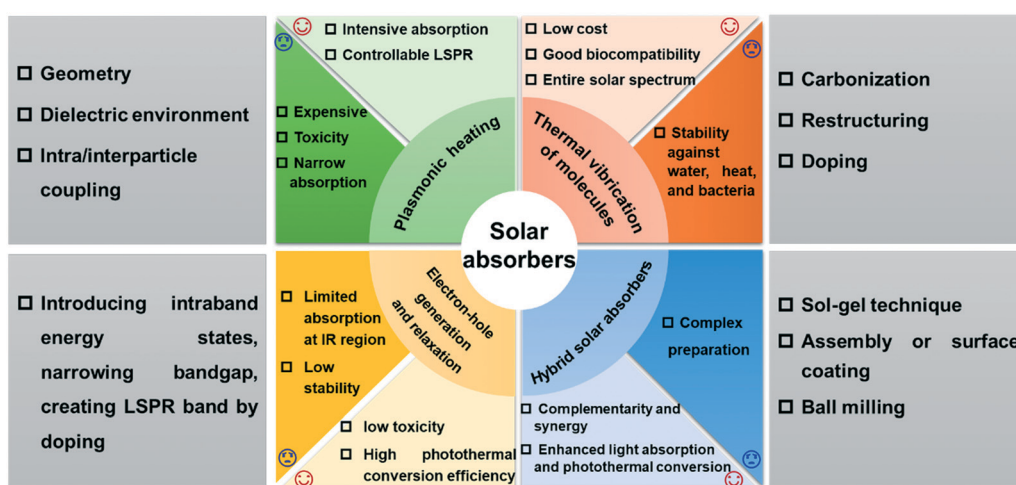


Fig. 14 Summary of the advantages (light-colored area), disadvantages (dark-colored area), and modulation strategies (grey box) of the four types of solar absorbers.

compatibility, allowing them to be deposited on various substrates. However, their long-term stability and scalable production are still challenging and required further exploration. As for semiconductors, they usually have high photothermal conversion efficiency and low toxicity, but the wide bandgaps impede their light absorption at the IR region, weakening the solar energy harvesting capacity. Under the circumstances, hybridization of two or more kinds of solar absorbers has been conducted to reinforce complementary advantages for high-performance solar evaporation.

In terms of highlighting the improvement of the solar absorber's optical properties, strategies in terms of thermal management and water transportation were discussed with typical examples. Although recent achievements on solar evaporation have been extensively demonstrated, there are still several enormous challenges that need to be addressed, aiming at narrowing the gap between laboratory research and practical applications in real life.

First, since quite a few solar absorbers have achieved high solar absorptivity (>90%), further development of novel solar absorbing agents should focus not only on the enhancement of optical properties, but also on the cost reduction, scalable production, anti-salting and anti-fouling properties, long-term stability and durability in natural water sources, recyclability, flexibility, and environmental compatibility.

Second, although we overviewed the merits and drawbacks of abundant solar absorbers in this review, it is difficult to directly compare the solar-to-heat conversion and water evaporation performances due to the discrepant experimental parameters, setups, measurement techniques, and calculation approaches in different literature reports. Thus, it is important to establish generally accepted guidelines referring to these aspects to standardize the performance evaluations of solar absorbers and evaporation systems. More than that, the energy conversion efficiency and water evaporation rate are not only determined by solar absorbers, so they cannot actually reflect the performance of solar absorbers. Therefore, it is recommended to develop new techniques for quantifying the solar to heat conversion of solar absorbers.

Third, most solar evaporators are not suitable for treating VOC-containing water sources, because these organic pollutants will be collected along with the distilled water and can even be enriched, leading to secondary pollution. Therefore, how to intercept VOCs during water evaporation without compromising the efficiency is worthwhile to investigate.

Fourth, it may not be enough to largely increase the evaporation rate only by suppressing the thermal losses, since there is not much room from the theoretical limit (100%). As a result, new directions, such as taking advantage of latent heat and environmental energy, should be further explored.

Fifth, most of the current experiments are usually performed in an open space, so that the reported evaporation

efficiencies are overestimated compared to the situation in a sealed space when water condensation and collection are considered. In this case, it is essential to develop strategies for mitigating the adverse effects on the evaporation process, e.g., high humidity in the confined space and increased reflection of incident light induced by the condensed water covering on the roof.

Sixth, solar irradiation is not always constant in nature due to the day-night cycle and changeable weather; therefore, it is important to design intelligent solar-responsive evaporation systems or equip water evaporation systems with an energy storage unit to maximize the utilization of solar energy.

Conflicts of interest

The authors declare no conflict of interest.

Acknowledgements

This work was supported by the National Natural Science Foundation of China (No. 42022056, 42192574, 41877389, 42077394, 22176196), Revitalize Liaoning Talents Program (XLYC1907136, XLYC1907118, XLYC2007124), the Hundreds Talents Program of the Chinese Academy of Sciences awarded to Xuejiao Zhang (2015–2021), Liaoning BaiQianWan Talents Program, and Liaoning Province Natural Science Foundation (2020-YQ-10), GDAS' Project of Science and Technology Development (2020GDASYL-20200101002, 2021GDASYL-20210302003), and Guangdong Foundation for Program of Science and Technology Research (No. 2019B121201004, 2020B1212060048).

References

- 1 S. K. Patel, C. L. Ritt, A. Deshmukh, Z. Wang, M. Qin, R. Epsztein and M. Elimelech, The relative insignificance of advanced materials in enhancing the energy efficiency of desalination technologies, *Energy Environ. Sci.*, 2020, **13**, 1694–1710.
- 2 S. Cao, P. Rathi, X. Wu, D. Ghim, Y.-S. Jun and S. Singamaneni, Cellulose Nanomaterials in Interfacial Evaporators for Desalination: A “Natural” Choice, *Adv. Mater.*, 2020, 202000922.
- 3 K. Xu, C. Wang, Z. Li, S.-M. Wu and W. Jiulong, Salt Mitigation Strategies of Solar Driven Interfacial Desalination, *Adv. Funct. Mater.*, 2020, 2007855.
- 4 T. S. Otitoju, R. Ari and A. L. Ahmad, Progress in the modification of reverse osmosis (RO) membranes for enhanced performance, *J. Ind. Eng. Chem.*, 2018, **67**, 52–71.
- 5 B. Wu, A. Maleki, F. Pourfayaz and M. A. Rosen, Optimal design of stand-alone reverse osmosis desalination driven by a photovoltaic and diesel generator hybrid system, *Sol. Energy*, 2018, **163**, 91–103.
- 6 A. K. Singh, S. Kumar, M. Bhushan and V. K. Shahi, High performance cross-linked dehydro-halogenated poly(vinylidene fluoride-co-hexafluoro propylene) based anion-

- exchange membrane for water desalination by electrodialysis, *Sep. Purif. Technol.*, 2020, **234**, 116078.
- 7 L. Eykens, K. De Sitter, S. Paulussen, M. Dubreuil, C. Dotremont, L. Pinoy and B. Van der Bruggen, Atmospheric plasma coatings for membrane distillation, *J. Membr. Sci.*, 2018, **554**, 175–183.
 - 8 P. Wang, Emerging investigator series: the rise of nano-enabled photothermal materials for water evaporation and clean water production by sunlight, *Environ. Sci.: Nano*, 2018, **5**, 1078–1089.
 - 9 L. Zhu, M. Gao, C. K. N. Peh and G. W. Ho, Recent progress in solar-driven interfacial water evaporation: Advanced designs and applications, *Nano Energy*, 2019, **57**, 507–518.
 - 10 G. Ni, G. Li, S. Boriskina, H. Li, W. Yang, T. Zhang and G. Chen, Steam generation under one sun enabled by a floating structure with thermal concentration, *Nat. Energy*, 2016, **1**, 16126.
 - 11 C. Chen, Y. Kuang and L. Hu, Challenges and Opportunities for Solar Evaporation, *Joule*, 2019, **3**(3), 683–718.
 - 12 J. Kim, S. Lee, S. J. Kang and T. Kim, Materials and design of nanostructured broadband light absorbers for advanced light-to-heat conversion, *Nanoscale*, 2018, **10**(46), 21555–21574.
 - 13 Z. Xie, Y. Duo, Z. Lin, T. Fan, C. Xing, L. Yu, R. Wang, M. Qiu, Y. Zhang, Y. Zhao, X. Yan and H. Zhang, The Rise of 2D Photothermal Materials beyond Graphene for Clean Water Production, *Adv. Sci.*, 2020, **7**(5), 1902236.
 - 14 S. Chaule, J. Hwang, S.-J. Ha, J. Kang, J.-C. Yoon and J.-H. Jang, Rational Design of a High Performance and Robust Solar Evaporator via 3D-Printing Technology, *Adv. Mater.*, 2021, **33**(38), 2102649.
 - 15 A. O. Govorov and H. H. Richardson, Generating heat with metal nanoparticles, *Nano Today*, 2007, **2**(1), 30–38.
 - 16 L. Zhu, M. Gao, C. K. N. Peh and G. W. Ho, Solar-driven photothermal nanostructured materials designs and prerequisites for evaporation and catalysis applications, *Mater. Horiz.*, 2018, **5**(3), 323–343.
 - 17 F. Cao, K. McEnaney, G. Chen and Z. Ren, A review of cermet-based spectrally selective solar absorbers, *Energy Environ. Sci.*, 2014, **7**(5), 1615–1627.
 - 18 T. Bostrom, E. Wackelgard and G. Westin, Solution-chemical derived nickel-alumina coatings for thermal solar absorbers, *Sol. Energy*, 2003, **74**(6), 497–503.
 - 19 Z. Deng, P.-F. Liu, J. Zhou, L. Miao, Y. Peng, H. Su, P. Wang, X. Wang, W. Cao, F. Jiang, L. Sun and S. Tanemura, A Novel Ink-Stained Paper for Solar Heavy Metal Treatment and Desalination, *Sol. RRL*, 2018, **2**(10), 1800073.
 - 20 G. Ni, G. Li, S. V. Boriskina, H. Li, W. Yang, T. Zhang and G. Chen, Steam generation under one sun enabled by a floating structure with thermal concentration, *Nat. Energy*, 2016, **1**(9), 16126.
 - 21 H. Ghasemi, G. Ni, A. M. Marconnet, J. Loomis, S. Yerci, N. Miljkovic and G. Chen, Solar steam generation by heat localization, *Nat. Commun.*, 2014, **5**, 4449.
 - 22 P. Zhang, Q. Liao, H. Yao, Y. Huang, H. Cheng and L. Qu, Direct solar steam generation system for clean water production, *Energy Storage Mater.*, 2019, **18**, 429–446.
 - 23 J. Zhou, Y. Gu, P. Liu, P. Wang, L. Miao, J. Liu, A. Wei, X. Mu, J. Li and J. Zhu, Development and Evolution of the System Structure for Highly Efficient Solar Steam Generation from Zero to Three Dimensions, *Adv. Funct. Mater.*, 2019, 1903255.
 - 24 Y. Yuan, C. Dong, J. Gu, Q. Liu, J. Xu, C. Zhou, G. Song, W. Chen, L. Yao and D. Zhang, A Scalable Nickel-Cellulose Hybrid Metamaterial with Broadband Light Absorption for Efficient Solar Distillation, *Adv. Mater.*, 2020, e1907975.
 - 25 O. Neumann, A. S. Urban, J. Day, S. Lal, P. Nordlander and N. J. Halas, Solar Vapor Generation Enabled by Nanoparticles, *ACS Nano*, 2013, **7**(1), 42–49.
 - 26 G. Ni, N. Miljkovic, H. Ghasemi, X. Huang, S. V. Boriskina, C.-T. Lin, J. Wang, Y. Xu, M. M. Rahman, T. Zhang and G. Chen, Volumetric solar heating of nanofluids for direct vapor generation, *Nano Energy*, 2015, **17**, 290–301.
 - 27 A. E. Kabeel and S. A. El-Agouz, Review of researches and developments on solar stills, *Desalination*, 2011, **276**(1–3), 1–12.
 - 28 P. Tao, G. Ni, C. Song, W. Shang, J. Wu, J. Zhu, G. Chen and T. Deng, Solar-driven interfacial evaporation, *Nat. Energy*, 2018, **3**(12), 1031–1041.
 - 29 X. Li, J. Li, J. Lu, N. Xu, C. Chen, X. Min, B. Zhu, H. Li, L. Zhou, S. Zhu, T. Zhang and J. Zhu, Enhancement of Interfacial Solar Vapor Generation by Environmental Energy, *Joule*, 2018, **2**(7), 1331–1338.
 - 30 A. H. Elsheikh, S. W. Sharshir, M. K. Ahmed Ali, J. Shaibo, E. M. A. Edreis, T. Abdelhamid, C. Du and Z. Haiou, Thin film technology for solar steam generation: A new dawn, *Sol. Energy*, 2019, **177**, 561–575.
 - 31 X. Wang, Y. He, X. Liu, G. Cheng and J. Zhu, Solar steam generation through bio-inspired interface heating of broadband-absorbing plasmonic membranes, *Appl. Energy*, 2017, **195**, 414–425.
 - 32 L. Zhu, M. Gao, C. K. N. Peh, X. Wang and G. W. Ho, Self-Contained Monolithic Carbon Sponges for Solar-Driven Interfacial Water Evaporation Distillation and Electricity Generation, *Adv. Energy Mater.*, 2018, **8**(16), 1702149.
 - 33 G. Liu, J. Xu and K. Wang, Solar water evaporation by black photothermal sheets, *Nano Energy*, 2017, **41**, 269–284.
 - 34 M. L. Brongersma, N. J. Halas and P. Nordlander, Plasmon-induced hot carrier science and technology, *Nat. Nanotechnol.*, 2015, **10**(1), 25–34.
 - 35 S. Linic, U. Aslam, C. Boerigter and M. Morabito, Photochemical transformations on plasmonic metal nanoparticles, *Nat. Mater.*, 2015, **14**(6), 567–576.
 - 36 J. A. Webb and R. Bardhan, Emerging advances in nanomedicine with engineered gold nanostructures, *Nanoscale*, 2014, **6**(5), 2502–2530.
 - 37 J. Liang, H. Liu, J. Yu, L. Zhou and J. Zhu, Plasmon-enhanced solar vapor generation, *Nanophotonics*, 2019, **8**(5), 771–786.
 - 38 H. Wang, L. Miao and S. Tanemura, Morphology Control of Ag Polyhedron Nanoparticles for Cost-Effective and Fast Solar Steam Generation, *Sol. RRL*, 2017, **1**(3–4), 1600023.
 - 39 M.-J. Chiu and L.-K. Chu, Quantifying the photothermal efficiency of gold nanoparticles using tryptophan as an in

- situ fluorescent thermometer, *Phys. Chem. Chem. Phys.*, 2015, **17**(26), 17090–17100.
- 40 N. R. Jana, L. Gearheart and C. J. Murphy, Seeding Growth for Size Control of 5–40 nm Diameter Gold Nanoparticles, *Langmuir*, 2001, **17**(22), 6782–6786.
- 41 J. N. Anker, W. P. Hall, O. Lyandres, N. C. Shah, J. Zhao and R. P. Van Duyne, Biosensing with plasmonic nanosensors, *Nat. Mater.*, 2008, **7**(6), 442–453.
- 42 J. Chen, J. Feng, Z. Li, P. Xu, X. Wang, W. Yin, M. Wang, X. Ge and Y. Yin, Space-Confining Seeded Growth of Black Silver Nanostructures for Solar Steam Generation, *Nano Lett.*, 2019, **19**(1), 400–407.
- 43 S. Ishii, R. P. Sugavaneshwar and T. Nagao, Titanium Nitride Nanoparticles as Plasmonic Solar Heat Transducers, *J. Phys. Chem. C*, 2016, **120**(4), 2343–2348.
- 44 O. Neumann, C. Feronti, A. D. Neumann, A. Dong, K. Schell, B. Lu, E. Kim, M. Quinn, S. Thompson, N. Grady, P. Nordlander, M. Oden and N. J. Halas, Compact solar autoclave based on steam generation using broadband light-harvesting nanoparticles, *Proc. Natl. Acad. Sci. U. S. A.*, 2013, **110**(29), 11677–11681.
- 45 S. Link, M. B. Mohamed and M. A. El-Sayed, Simulation of the Optical Absorption Spectra of Gold Nanorods as a Function of Their Aspect Ratio and the Effect of the Medium Dielectric Constant, *J. Phys. Chem. B*, 1999, **103**(16), 3073–3077.
- 46 C. J. Murphy, T. K. Sau, A. Gole, C. J. Orendorff, J. Gao, L. Gou, S. E. Hunyadi and T. Li, Anisotropic Metal Nanoparticles: Synthesis, Assembly, and Optical Applications, *J. Phys. Chem. B*, 2005, **109**(29), 13857–13870.
- 47 G. Baffou, R. Quidant and C. Girard, Heat generation in plasmonic nanostructures: Influence of morphology, *Appl. Phys. Lett.*, 2009, **94**, 153109.
- 48 P. K. Jain and M. A. ElSayed, Universal scaling of plasmon coupling in metal nanostructures: Extension from particle pairs to nanoshells, *Nano Lett.*, 2007, **7**(9), 2854–2858.
- 49 M. J. Banholzer, N. Harris, J. E. Millstone, G. Schatz and C. A. Mirkin, Abnormally large plasmonic shifts in silica-protected gold triangular nanoprisms, *J. Phys. Chem. C*, 2010, **114**, 7521–7526.
- 50 B. Sharma and M. K. Rabinal, Plasmon based metal-graphene nanocomposites for effective solar vaporization, *J. Alloys Compd.*, 2017, **690**, 57–62.
- 51 K. L. Kelly, E. A. Coronado, L. L. Zhao and G. C. Schatz, The Optical Properties of Metal Nanoparticles: The Influence of Size, Shape, and Dielectric Environment, *J. Phys. Chem. B*, 2003, **107**(3), 668–677.
- 52 M. Ryeenga, C. M. Cobley, J. Zeng, W. Li, C. H. Moran, Q. Zhang, D. Qin and Y. Xia, Controlling the synthesis and assembly of silver nanostructures for plasmonic applications, *Chem. Rev.*, 2011, **111**(6), 3669–3712.
- 53 C. Langhammer, M. Schwind, B. H. Kasemo and I. Zoric, Localized Surface Plasmon Resonances in Aluminum Nanodisks, *Nano Lett.*, 2008, **8**(5), 1461–1471.
- 54 M. W. Knight, N. S. King, L. Liu, H. O. Everitt, P. Nordlander and N. J. Halas, Aluminum for Plasmonics, *ACS Nano*, 2014, **8**(1), 834–840.
- 55 L. Zhou, Y. Tan, J. Wang, W. Xu, Y. Yuan, W. Cai, S. Zhu and J. Zhu, 3D self-assembly of aluminium nanoparticles for plasmon-enhanced solar desalination, *Nat. Photonics*, 2016, **10**(6), 393–398.
- 56 J. M. Sanz, D. Ortiz, R. A. D. La Osa, J. M. Saiz, F. J. Gonzalez, A. S. Brown, M. Losurdo, H. O. Everitt and F. Moreno, UV Plasmonic Behavior of Various Metal Nanoparticles in the Near- and Far-Field Regimes: Geometry and Substrate Effects, *J. Phys. Chem. C*, 2013, **117**(38), 19606–19615.
- 57 J. Q. Xi, M. F. Schubert, J. K. Kim, E. F. Schubert, M. Chen, S. Lin, W. Liu and J. A. Smart, Optical thin-film materials with low refractive index for broadband elimination of Fresnel reflection, *Nat. Photonics*, 2007, **1**(3), 176–179.
- 58 G. H. Chan, J. Zhao, E. M. Hicks, G. C. Schatz and R. P. Van Duyne, Plasmonic Properties of Copper Nanoparticles Fabricated by Nanosphere Lithography, *Nano Lett.*, 2007, **7**(7), 1947–1952.
- 59 Y. Lin, Z. Chen, L. Fang, M. Meng, Z. Liu, Y. Di, W. Cai, S. Huang and Z. Gan, Copper nanoparticles with near-unity, omnidirectional, and broadband optical absorption for highly efficient solar steam generation, *Nanotechnology*, 2019, **30**(1), 015402.
- 60 J. Planelles, A. W. Achstein, R. Scott, N. Owschimikow, U. Woggon and J. I. Climente, Tuning Intraband and Interband Transition Rates via Excitonic Correlation in Low-Dimensional Semiconductors, *ACS Photonics*, 2018, **5**(9), 3680–3688.
- 61 W. S. Choi, S. S. A. Seo, K. W. Kim, T. W. Noh, M. Y. Kim and S. Shin, Dielectric constants of Ir, Ru, Pt, and IrO_2 : Contributions from bound charges, *Phys. Rev. B: Condens. Matter Mater. Phys.*, 2006, **74**(20), 205117.
- 62 U. Aslam, V. G. Rao, S. Chavez and S. Linic, Catalytic conversion of solar to chemical energy on plasmonic metal nanostructures, *Nat. Catal.*, 2018, **1**(9), 656–665.
- 63 M. A. Malone, A. Luthra, D. Lioi and J. V. Coe, Developing Plasmonics Under the Infrared Microscope: From Ni Nanoparticle Arrays to Infrared Micromesh, *J. Phys. Chem. Lett.*, 2012, **3**(13), 1774–1782.
- 64 D. Wu, D. Qu, W. Jiang, G. Chen, L. An, C. Zhuang and Z. Sun, Self-floating nanostructured Ni-NiOx/Ni foam for solar thermal water evaporation, *J. Mater. Chem. A*, 2019, **7**(14), 8485–8490.
- 65 C. Ma, J. Yan, Y. Huang, C. Wang and G. Yang, The optical duality of tellurium nanoparticles for broadband solar energy harvesting and efficient photothermal conversion, *Sci. Adv.*, 2018, **4**(8), eaas9894.
- 66 J. Guo, J. Zhao, D. Huang, Y. Wang, F. Zhang, Y. Ge, Y. Song, C. Xing, D. Fan and H. Zhang, Two-dimensional tellurium-polymer membrane for ultrafast photonics, *Nanoscale*, 2019, **11**(13), 6235–6242.

- 67 C. Xing, D. Huang, S. Chen, Q. Huang, C. Zhou, Z. Peng, J. Li, X. Zhu, Y. Liu, Z. Liu, H. Chen, J. Zhao, J. Li, L. Liu, F. Cheng, D. Fan and H. Zhang, Engineering Lateral Heterojunction of Selenium-Coated Tellurium Nanomaterials toward Highly Efficient Solar Desalination, *Adv. Sci.*, 2019, **6**(19), 1900531.
- 68 M. Naguib, M. Kurtoglu, V. Presser, J. Lu, J. Niu, M. Heon, L. Hultman, Y. Gogotsi and M. W. Barsoum, Two-Dimensional Nanocrystals Produced by Exfoliation of Ti_3AlC_2 , *ChemInform*, 2011, **42**(52), 4248–4253.
- 69 M. Khazaei, M. Arai, T. Sasaki, C. Chung, N. S. Venkataraman, M. Estili, Y. Sakka and Y. Kawazoe, Novel Electronic and Magnetic Properties of Two-Dimensional Transition Metal Carbides and Nitrides, *Adv. Funct. Mater.*, 2013, **23**(17), 2185–2192.
- 70 B. Anasori, Y. Xie, M. Beidaghi, J. Lu, B. C. Hosler, L. Hultman, P. R. C. Kent, Y. Gogotsi and M. W. Barsoum, Two-Dimensional, Ordered, Double Transition Metals Carbides (MXenes), *ACS Nano*, 2015, **9**(10), 9507–9516.
- 71 H. Lin, X. Wang, L. Yu, Y. Chen and J. Shi, Two-Dimensional Ultrathin MXene Ceramic Nanosheets for Photothermal Conversion, *Nano Lett.*, 2017, **17**(1), 384–391.
- 72 R. Li, L. Zhang, L. Shi and P. Wang, MXene Ti_3C_2 : An Effective 2D Light-to-Heat Conversion Material, *ACS Nano*, 2017, **11**(4), 3752–3759.
- 73 Q. Zhang, G. Yi, Z. Fu, H. Yu, S. Chen and X. Quan, Vertically Aligned Janus MXene-Based Aerogels for Solar Desalination with High Efficiency and Salt Resistance, *ACS Nano*, 2019, **13**(11), 13196–13207.
- 74 Q. Zhang, Z. Fu, H. Yu and S. Chen, Nanoplaing of a SnO_2 thin-film on MXene-based sponge for stable and efficient solar energy conversion, *J. Mater. Chem. A*, 2020, **8**(16), 8065–8074.
- 75 J. Zhao, Y. Yang, C. Yang, Y. Tian, Y. Han, J. Liu, X. Yin and W. Que, A hydrophobic surface enabled salt-blocking 2D Ti_3C_2 MXene membrane for efficient and stable solar desalination, *J. Mater. Chem. A*, 2018, **6**(33), 16196–16204.
- 76 C. Dai, Y. Chen, X. Jing, L. Xiang, D. Yang, H. Lin, Z. Liu, X. Han and R. Wu, Two-Dimensional Tantalum Carbide (MXenes) Composite Nanosheets for Multiple Imaging-Guided Photothermal Tumor Ablation, *ACS Nano*, 2017, **11**(12), 12696–12712.
- 77 H. Lin, Y. Wang, S. Gao, Y. Chen and J. Shi, Theranostic 2D Tantalum Carbide (MXene), *Adv. Mater.*, 2018, **30**(4), 1703284.
- 78 U. Guler, V. M. Shalaev and A. Boltasseva, Nanoparticle plasmonics: going practical with transition metal nitrides, *Mater. Today*, 2015, **18**(4), 227–237.
- 79 W. Li, U. Guler, N. Kinsey, G. V. Naik, A. Boltasseva, J. Guan, V. M. Shalaev and A. V. Kildishev, Refractory Plasmonics with Titanium Nitride: Broadband Metamaterial Absorber, *Adv. Mater.*, 2014, **26**(47), 7959–7965.
- 80 U. Guler, J. C. Ndukaife, G. V. Naik, A. G. A. Nnanna, A. V. Kildishev, V. M. Shalaev and A. Boltasseva, Local Heating with Lithographically Fabricated Plasmonic Titanium Nitride Nanoparticles, *Nano Lett.*, 2013, **13**(12), 6078–6083.
- 81 A. Agrawal, R. W. Johns and D. J. Milliron, Control of Localized Surface Plasmon Resonances in Metal Oxide Nanocrystals, *Annu. Rev. Mater. Res.*, 2017, **47**(1), 1–31.
- 82 G. Song, J. Shen, F. Jiang, R. Hu, W. Li, L. An, R. Zou, Z. Chen, Z. Qin and J. Hu, Hydrophilic molybdenum oxide nanomaterials with controlled morphology and strong plasmonic absorption for photothermal ablation of cancer cells, *ACS Appl. Mater. Interfaces*, 2014, **6**(6), 3915–3922.
- 83 Z. Li, M. Zheng, N. Wei, Y. Lin, W. Chu, R. Xu, H. Wang, J. Tian and H. Cui, Broadband-absorbing WO_3-x nanorod-decorated wood evaporator for highly efficient solar-driven interfacial steam generation, *Sol. Energy Mater. Sol. Cells*, 2020, **205**, 110254.
- 84 J. Yan, P. Liu, C. Ma, Z. Lin and G. Yang, Plasmonic near-touching titanium oxide nanoparticles to realize solar energy harvesting and effective local heating, *Nanoscale*, 2016, **8**(16), 8826–8838.
- 85 A. H. Odda, Y. Xu, J. Lin, G. Wang, N. Ullah, A. Zeb, K. Liang, L. Wen and A. Xu, Plasmonic MoO_3-x nanoparticles incorporated in Prussian blue frameworks exhibit highly efficient dual photothermal/photodynamic therapy, *J. Mater. Chem. B*, 2019, **7**(12), 2032–2042.
- 86 Q. Yin, L. Tan, Q. Lang, X. Ke, L. Bai, K. Guo, R. Qiao and S. Bai, Plasmonic molybdenum oxide nanosheets supported silver nanocubes for enhanced near-infrared antibacterial activity: Synergism of photothermal effect, silver release and photocatalytic reactions, *Appl. Catal., B*, 2018, **224**, 671–680.
- 87 Q. Huang, S. Hu, J. Zhuang and X. Wang, MoO_3-x -Based Hybrids with Tunable Localized Surface Plasmon Resonances: Chemical Oxidation Driving Transformation from Ultrathin Nanosheets to Nanotubes, *Chem. – Eur. J.*, 2012, **18**(48), 15283–15287.
- 88 G. Li, S. Zhang, C. Guo and S. Liu, Absorption and electrochromic modulation of near-infrared light: realized by tungsten suboxide, *Nanoscale*, 2016, **8**(18), 9861–9868.
- 89 J. Li, Y. Ye, L. Ye, F. Su, Z. Ma, J. Huang, H. Xie, D. E. Doronkin, A. Zimina and J. Grunwaldt, Sunlight induced photo-thermal synergistic catalytic CO_2 conversion via localized surface plasmon resonance of MoO_{3-x} , *J. Mater. Chem.*, 2019, **7**(6), 2821–2830.
- 90 A. O. Govorov, H. Zhang and Y. K. Gunko, Theory of Photoinjection of Hot Plasmonic Carriers from Metal Nanostructures into Semiconductors and Surface Molecules, *J. Phys. Chem. C*, 2013, **117**(32), 16616–16631.
- 91 R. Sundararaman, P. Narang, A. S. Jermyn, W. A. Goddard and H. A. Atwater, Theoretical predictions for hot-carrier generation from surface plasmon decay, *Nat. Commun.*, 2014, **5**(1), 5788.
- 92 S. Naseem, C.-M. Wu and T. F. Chala, Photothermal-responsive tungsten bronze/recycled cellulose triacetate porous fiber membranes for efficient light-driven interfacial water evaporation, *Sol. Energy*, 2019, **194**, 391–399.
- 93 Q. Zhu, K. Ye, W. Zhu, W. Xu, C. Zou, L. Song, E. Sharman, L. Wang, S. Jin, G. Zhang, Y. Luo and J. Jiang, A Hydrogenated Metal Oxide with Full Solar Spectrum

- Absorption for Highly Efficient Photothermal Water Evaporation, *J. Phys. Chem. Lett.*, 2020, **11**(7), 2502–2509.
- 94 M. Yang, C. F. Tan, W. Lu, K. Zeng and G. W. Ho, Spectrum Tailored Defective 2D Semiconductor Nanosheets Aerogel for FulOE Spectrue Driven Photothermal Water Evaporation and Photochemical Degradation, *Adv. Funct. Mater.*, 2020, **30**, 2004460.
- 95 Y. Zhao and C. Burda, Development of plasmonic semiconductor nanomaterials with copper chalcogenides for a future with sustainable energy materials, *Energy Environ. Sci.*, 2012, **5**, 5564–5576.
- 96 C. Mu, Y. Song, K. Deng, S. Lin, Y. Bi, F. Scarpa and D. Crouse, High Solar Desalination Efficiency Achieved with 3D Cu₂ZnSnS₄Nanosheet-Assembled Membranes, *Adv. Sustainable Syst.*, 2017, **1**(10), 1700064.
- 97 Y. Yang, H. Zhao, Z. Yin, J. Zhao, X. Yin, N. Li, D. Yin, Y. Li, B. Lei, Y. Du and W. Que, A general salt-resistant hydrophilic/hydrophobic nanoporous double layer design for efficient and stable solar water evaporation distillation, *Mater. Horiz.*, 2018, **5**(6), 1143–1150.
- 98 L. Zhou, Y. Tan, D. Ji, B. Zhu, P. Zhang, J. Xu, Q. Gan, Z. Yu and J. Zhu, Self-assembly of highly efficient, broadband plasmonic absorbers for solar steam generation, *Sci. Adv.*, 2016, **2**(4), e1501227.
- 99 K. Bae, G. Kang, S. K. Cho, W. Park, K. Kim and W. J. Padilla, Flexible thin-film black gold membranes with ultrabroadband plasmonic nanofocusing for efficient solar vapour generation, *Nat. Commun.*, 2015, **6**, 10103.
- 100 X. Song, H. Song, N. Xu, H. Yang, L. Zhou, L. Yu, J. Zhu, J. Xu and K. Chen, Omnidirectional and effective salt-rejecting absorber with rationally designed nanoarchitecture for efficient and durable solar vapour generation, *J. Mater. Chem. A*, 2018, **6**(45), 22976–22986.
- 101 M. Kaur, S. Ishii, S. L. Shinde and T. Nagao, All-Ceramic Microfibrous Solar Steam Generator: TiN Plasmonic Nanoparticle-Loaded Transparent Microfibers, *ACS Sustainable Chem. Eng.*, 2017, **5**(10), 8523–8528.
- 102 Z. Wang, J. Zhou, Y. Zhang, W. Zhu and Y. Li, Accessing Highly Efficient Photothermal Conversion with Stable Open-Shell Aromatic Nitric Acid Radicals, *Angew. Chem.*, 2022, e202113653.
- 103 P. Zhang, J. Li, L. Lv, Y. Zhao and L. Qu, Vertically Aligned Graphene Sheets Membrane for Highly Efficient Solar Thermal Generation of Clean Water, *ACS Nano*, 2017, **11**(5), 5087–5093.
- 104 Z. Yang, L. Ci, J. A. Bur, S. Lin and P. M. Ajayan, Experimental observation of an extremely dark material made by a low-density nanotube array, *Nano Lett.*, 2008, **8**(2), 446–451.
- 105 M. Liu, X. Yin, E. Ulin-Avila, B. Geng, T. Zentgraf, L. Ju, F. Wang and X. Zhang, A graphene-based broadband optical modulator, *Nature*, 2011, **474**, 64–67.
- 106 F. Zhao, Y. Guo, X. Zhou, W. Shi and G. Yu, Materials for solar-powered water evaporation, *Nat. Rev. Mater.*, 2020, **5**, 388–401.
- 107 Q. Liao, P. Zhang, H. Yao, H. Cheng, C. Li and L. Qu, Reduced Graphene Oxide-Based Spectrally Selective Absorber with an Extremely Low Thermal Emittance and High Solar Absorptance, *Adv. Sci.*, 2020, **7**(8), 1903125.
- 108 W. Tu, Z. Wang, Q. Wu, H. Huang, Y. Liu, M. Shao, B. Yao and Z. Kang, Tree-inspired ultra-rapid steam generation and simultaneous energy harvesting under weak illumination, *J. Mater. Chem. A*, 2020, **8**(20), 10260–10268.
- 109 D. W. Boukhvalov, M. I. Katsnelson and Y. Son, Origin of Anomalous Water Permeation through Graphene Oxide Membrane, *Nano Lett.*, 2013, **13**(8), 3930–3935.
- 110 L. Tian, P. Anilkumar, L. Cao, C. Y. Kong, M. J. Meziani, H. Qian, L. M. Veca, T. J. Thorne, K. N. Tackett and T. Edwards, Graphene Oxides Dispersing and Hosting Graphene Sheets for Unique Nanocomposite Materials, *ACS Nano*, 2011, **5**(4), 3052–3058.
- 111 S. L. Loo, L. Vasquez, U. C. Paul, L. Campagnolo, A. Athanassiou and D. Fragouli, Solar-Driven Freshwater Generation from Seawater and Atmospheric Moisture Enabled by a Hydrophilic Photothermal Foam, *ACS Appl. Mater. Interfaces*, 2020, **12**(9), 10307–10316.
- 112 J. Yang, Y. Pang, W. Huang, S. K. Shaw, J. Schiffbauer, M. A. Pillers, X. Mu, S. Luo, T. Zhang and Y. Huang, Functionalized Graphene Enables Highly Efficient Solar Thermal Steam Generation, *ACS Nano*, 2017, **11**(6), 5510–5518.
- 113 X. Deng, Q. Nie, Y. Wu, H. Fang, P. Zhang and Y. Xie, Nitrogen-Doped Unusually Superwetting, Thermally Insulating, and Elastic Graphene Aerogel for Efficient Solar Steam Generation, *ACS Appl. Mater. Interfaces*, 2020, **12**(23), 26200–26212.
- 114 D. Li, X. Zhang, S. Zhang, D. Wang, Z.-Y. Wang, Y. Liu, X. Yu, Q. Zhao and B. Xing, A flexible and salt-rejecting electrospun film-based solar evaporator for economic, stable and efficient solar desalination and wastewater treatment, *Chemosphere*, 2020, 128916.
- 115 K. Mizuno, J. Ishii, H. Kishida, Y. Hayamizu, S. Yasuda, D. N. Futaba, M. Yumura and K. Hata, A black body absorber from vertically aligned single-walled carbon nanotubes, *Proc. Natl. Acad. Sci. U. S. A.*, 2009, **106**(15), 6044–6047.
- 116 Z. Yin, H. Wang, M. Jian, Y. Li, K. Xia, M. Zhang, C. Wang, Q. Wang, M. Ma, Q. S. Zheng and Y. Zhang, Extremely Black Vertically Aligned Carbon Nanotube Arrays for Solar Steam Generation, *ACS Appl. Mater. Interfaces*, 2017, **9**(34), 28596–28603.
- 117 C. Chen, Y. Li, J. Song, Z. Yang, Y. Kuang, E. Hitz, C. Jia, A. Gong, F. Jiang, J. Y. Zhu, B. Yang, J. Xie and L. Hu, Highly Flexible and Efficient Solar Steam Generation Device, *Adv. Mater.*, 2017, **29**(30), 1701756.
- 118 Y. Wang, H. Liu, C. Chen, Y. Kuang, J. Song, H. Xie, C. Jia, S. Kronthal, X. Xu, S. He and L. Hu, All Natural, High Efficient Groundwater Extraction via Solar Steam/Vapor Generation, *Adv. Sustainable Syst.*, 2019, **3**(1), 1800055.
- 119 R. Jiang, S. Cheng, L. Shao, Q. Ruan and J. Wang, Mass-Based Photothermal Comparison Among Gold Nanocrystals, PbS Nanocrystals, Organic Dyes, and Carbon Black, *J. Phys. Chem. C*, 2013, **117**(17), 8909–8915.

- 120 Y. Jin, J. Chang, Y. Shi, L. Shi, S. Hong and P. Wang, A highly flexible and washable nonwoven photothermal cloth for efficient and practical solar steam generation, *J. Mater. Chem. A*, 2018, **6**(17), 7942–7949.
- 121 W. Xu, X. Hu, S. Zhuang, Y. Wang, X. Li, L. Zhou, S. Zhu and J. Zhu, Flexible and Salt Resistant Janus Absorbers by Electrospinning for Stable and Efficient Solar Desalination, *Adv. Energy Mater.*, 2018, **8**(14), 1702884.
- 122 S. He, C. Chen, Y. Kuang, R. Mi, Y. Liu, Y. Pei, W. Kong, W. Gan, H. Xie, E. Hitz, C. Jia, X. Chen, A. Gong, J. Liao, J. Li, Z. J. Ren, B. Yang, S. Das and L. Hu, Nature-inspired salt resistant bimodal porous solar evaporator for efficient and stable water desalination, *Energy Environ. Sci.*, 2019, **12**(5), 1558–1567.
- 123 Y. Kuang, C. Chen, S. He, E. M. Hitz, Y. Wang, W. Gan, R. Mi and L. Hu, A High-Performance Self-Regenerating Solar Evaporator for Continuous Water Desalination, *Adv. Mater.*, 2019, **31**(23), e1900498.
- 124 M. Zhu, Y. Li, G. Chen, F. Jiang, Z. Yang, X. Luo, Y. Wang, S. D. Lacey, J. Dai, C. Wang, C. Jia, J. Wan, Y. Yao, A. Gong, B. Yang, Z. Yu, S. Das and L. Hu, Tree-Inspired Design for High-Efficiency Water Extraction, *Adv. Mater.*, 2017, **29**(44), 1704107.
- 125 H. Liu, C. Chen, G. Chen, Y. Kuang, X. Zhao, J. Song, C. Jia, X. Xu, E. Hitz, H. Xie, S. Wang, F. Jiang, T. Li, Y. Li, A. Gong, R. Yang, S. Das and L. Hu, High-Performance Solar Steam Device with Layered Channels: Artificial Tree with a Reversed Design, *Adv. Energy Mater.*, 2018, **8**(8), 1701616.
- 126 N. Xu, X. Hu, W. Xu, X. Li, L. Zhou, S. Zhu and J. Zhu, Mushrooms as Efficient Solar Steam-Generation Devices, *Adv. Mater.*, 2017, **29**(28), 1606762.
- 127 Q. Fang, T. Li, Z. Chen, H. Lin, P. Wang and F. Liu, Full Biomass-Derived Solar Stills for Robust and Stable Evaporation To Collect Clean Water from Various Water-Bearing Media, *ACS Appl. Mater. Interfaces*, 2019, **11**(11), 10672–10679.
- 128 Y. Zhang, S. K. Ravi and S. C. Tan, Food-derived carbonaceous materials for solar desalination and thermo-electric power generation, *Nano Energy*, 2019, **65**, 104006.
- 129 C. Tian, J. Liu, R. Ruan, X. Tian, X. Lai, L. Xing, Y. Su, W. Huang, Y. Cao and J. Tu, Sandwich Photothermal Membrane with Confined Hierarchical Carbon Cells Enabling High-Efficiency Solar Steam Generation, *Small*, 2020, **16**(23), 2000573.
- 130 Q. Ding, C. Guan, H. Li, M. Shi, W. Yang, H. Yan, X. Zuo, Y. An, S. Ramakrishna, P. Mohankumar and F. Zhang, Solar-driven interfacial evaporation based on double-layer polylactic acid fibrous membranes loading Chinese ink nanoparticles, *Sol. Energy*, 2020, **195**, 636–643.
- 131 H. Wang, W. Yang, L. Cheng, C. Guan and H. Yan, Chinese ink: High performance nanofluids for solar energy, *Sol. Energy Mater. Sol. Cells*, 2018, **176**, 374–380.
- 132 H. C. Yang, Z. Chen, Y. Xie, J. Wang, J. W. Elam, W. Li and S. B. Darling, Chinese Ink: A Powerful Photothermal Material for Solar Steam Generation, *Adv. Mater. Interfaces*, 2018, **6**(1), 1801252.
- 133 Z. Li, J. Zhang, S. Zang, C. Yang, Y. Liu, F. Jing, H. Jing, J. Hu, C. Wang and Y. Zhou, Engineering controllable water transport of biosafety cuttlefish juice solar absorber toward remarkably enhanced solar-driven gas-liquid interfacial evaporation, *Nano Energy*, 2020, **73**, 104834.
- 134 S. Hong, Y. S. Na, S. Choi, I. T. Song, W. Y. Kim and H. Lee, Non-Covalent Self-Assembly and Covalent Polymerization Co-Contribute to Polydopamine Formation, *Adv. Funct. Mater.*, 2012, **22**(22), 4711–4717.
- 135 H. Lee, S. M. Dellatore, W. M. Miller and P. B. Messersmith, Mussel-Inspired Surface Chemistry for Multifunctional Coatings, *Science*, 2007, **318**(5849), 426–430.
- 136 X. Wu, G. Y. Chen, W. Zhang, X. Liu and H. Xu, A Plant-Transpiration-Process-Inspired Strategy for Highly Efficient Solar Evaporation, *Adv. Sustainable Syst.*, 2017, **1**(6), 1700046.
- 137 Q. Jiang, H. Gholami Derami, D. Ghim, S. Cao, Y.-S. Jun and S. Singamaneni, Polydopamine-filled bacterial nanocellulose as a biodegradable interfacial photothermal evaporator for highly efficient solar steam generation, *J. Mater. Chem. A*, 2017, **5**(35), 18397–18402.
- 138 X. Wu, L. Wu, J. Tan, G. Chen, G. Owens and H. Xu, Evaporation above a bulk water surface using an oil lamp inspired highly efficient solar-steam generation strategy, *J. Mater. Chem.*, 2018, **6**, 12267–12274.
- 139 Y. Zhang, X. Yin, B. Yu, X. Wang, Q. Guo and J. Yang, Recyclable Polydopamine-Functionalized Sponge for High-Efficiency Clean Water Generation with Dual-Purpose Solar Evaporation and Contaminant Adsorption, *ACS Appl. Mater. Interfaces*, 2019, **11**(35), 32559–32568.
- 140 M. Chen, X. Fang, S. Tang and N. Zheng, Polypyrrole nanoparticles for high-performance in vivo near-infrared photothermal cancer therapy, *Chem. Commun.*, 2012, **48**(71), 8934–8936.
- 141 Z. Zha, X. Yue, Q. Ren and Z. Dai, Uniform polypyrrole nanoparticles with high photothermal conversion efficiency for photothermal ablation of cancer cells, *Adv. Mater.*, 2013, **25**(5), 777–782.
- 142 L. Zhang, B. Tang, J. Wu, R. Li and P. Wang, Hydrophobic Light-to-Heat Conversion Membranes with Self-Healing Ability for Interfacial Solar Heating, *Adv. Mater.*, 2015, **27**(33), 4889–4894.
- 143 F. Zhao, X. Zhou, Y. Liu, Y. Shi, Y. Dai and G. Yu, Super Moisture-Absorbent Gels for All-Weather Atmospheric Water Harvesting, *Adv. Mater.*, 2019, **31**(10), e1806446.
- 144 X. Zhou, Y. Guo, F. Zhao and G. Yu, Hydrogels as an Emerging Material Platform for Solar Water Purification, *Acc. Chem. Res.*, 2019, 3244–3253.
- 145 F. Zhao, X. Zhou, Y. Shi, X. Qian, M. Alexander, X. Zhao, S. Mendez, R. Yang, L. Qu and G. Yu, Highly efficient solar vapour generation via hierarchically nanostructured gels, *Nat. Nanotechnol.*, 2018, **13**(6), 489–495.
- 146 W. Li, Z. Li, K. Bertelsmann and D. E. Fan, Portable Low-Pressure Solar Steaming-Collection Unisystem with Polypyrrole Origamis, *Adv. Mater.*, 2019, **31**(29), 1900720.
- 147 Y. Xu, H. Xu, Z. Zhu, H. Hou, J. Zuo, F. Cui, D. Liu and W. Wang, A mechanically durable, sustained corrosion-resistant

- photothermal nanofiber membrane for highly efficient solar distillation, *J. Mater. Chem. A*, 2019, **7**(39), 22296–22306.
- 148 X. Wang, Q. Liu, S. Wu, B. Xu and H. Xu, Multilayer Polypyrrole Nanosheets with Self-Organized Surface Structures for Flexible and Efficient Solar-Thermal Energy Conversion, *Adv. Mater.*, 2019, **31**(19), 1807716.
- 149 C. Li, D. Jiang, B. Huo, M. Ding, C. Huang, D. Jia, H. Li, C.-Y. Liu and J. Liu, Scalable and robust bilayer polymer foams for highly efficient and stable solar desalination, *Nano Energy*, 2019, **60**, 841–849.
- 150 Y. Xu, C. Tang, J. Ma, D. Liu, D. Qi, S. You, F. Cui, Y. Wei and W. Wang, Low-Tortuosity Water Microchannels Boosting Energy Utilization for High Water Flux Solar Distillation, *Environ. Sci. Technol.*, 2020, **54**(8), 5150–5158.
- 151 F. Ni, P. Xiao, N. Qiu, C. Zhang, Y. Liang, J. Gu, J. Xia, Z. Zeng, L. Wang, Q. Xue and T. Chen, Collective behaviors mediated multifunctional black sand aggregate towards environmentally adaptive solar-to-thermal purified water harvesting, *Nano Energy*, 2020, **68**, 104311.
- 152 Y. Xu, J. Wang, F. Yu, Z. Guo, H. Cheng, J. Yin, L. Yan and X. Wang, Flexible and Efficient Solar Thermal Generators Based on Polypyrrole Coated Natural Latex Foam for Multimedia Purification, *ACS Sustainable Chem. Eng.*, 2020, **8**(32), 12053–12062.
- 153 J. Yang, J. Choi, D. Bang, E. Kim, E. Lim, H. Park, J. Suh, K. Lee, K. Yoo, E. Kim, Y. Huh and S. Haam, Convertible organic nanoparticles for near-infrared photothermal ablation of cancer cells, *Angew. Chem., Int. Ed.*, 2011, **50**(2), 441–444.
- 154 X. Yin, Y. Zhang, Q. Guo, X. Cai, J. Xiao, Z. Ding and J. Yang, Macroporous Double-Network Hydrogel for High-Efficiency Solar Steam Generation Under 1 sun Illumination, *ACS Appl. Mater. Interfaces*, 2018, **10**(13), 10998–11007.
- 155 Y. Xu, S. Jin, H. Xu, A. Nagai and D. Jiang, Conjugated microporous polymers: design, synthesis and application, *Chem. Soc. Rev.*, 2013, **42**(20), 8012–8031.
- 156 A. Li, H. Sun, D. Tan, W. Fan, S. Wen, X. Qing, G. Li, S. Li and W. Deng, Superhydrophobic conjugated microporous polymers for separation and adsorption, *Energy Environ. Sci.*, 2011, **4**(6), 2062–2065.
- 157 X. Qian, B. Wang, Z. Zhu, H. Sun, F. Ren, P. Mu, C. Ma, W. Liang and A. Li, Novel N-rich porous organic polymers with extremely high uptake for capture and reversible storage of volatile iodine, *J. Hazard. Mater.*, 2017, **338**, 224–232.
- 158 H. Wei, F. Wang, H. Sun, Z. Zhu, C. Xiao, W. Liang, B. Yang, L. Chen and A. Li, Benzotriazole-based conjugated microporous polymers as efficient flame retardants with better thermal insulation properties, *J. Mater. Chem.*, 2018, **6**(18), 8633–8642.
- 159 P. Mu, W. Bai, Z. Zhang, J. He, H. Sun, Z. Zhu, W. Liang and A. Li, Robust aerogels based on conjugated microporous polymer nanotubes with exceptional mechanical strength for efficient solar steam generation, *J. Mater. Chem. A*, 2018, **6**(37), 18183–18190.
- 160 P. Mu, Z. Zhang, W. Bai, J. He, H. Sun, Z. Zhu, W. Liang and A. Li, Superwetting Monolithic Hollow-Carbon-
- Nanotubes Aerogels with Hierarchically Nanoporous Structure for Efficient Solar Steam Generation, *Adv. Energy Mater.*, 2019, **9**(1), 1802158.
- 161 J. Zhang, Y. Yang, J. Zhao, Z. Dai, W. Liu, C. Chen, S. Gao, D. A. Golosov, S. M. Zavadski and S. N. Melnikov, Shape tailored Cu₂ZnSnS₄ nanosheet aggregates for high efficiency solar desalination, *Mater. Res. Bull.*, 2019, **118**, 110529.
- 162 S. Tian, Z. Huang, J. Tan, X. Cui, Y. Xiao, Y. Wan, X. Li, Q. Zhao, S. Li and C.-S. Lee, Manipulating Interfacial Charge-Transfer Absorption of Cocrystal Absorber for Efficient Solar Seawater Desalination and Water Purification, *ACS Energy Lett.*, 2020, **5**(8), 2698–2705.
- 163 H. Li, H. Wen, J. Li, J. Huang, D. Wang and B. Z. Tang, Doping AIE Photothermal Molecule into All-Fiber Aerogel with Self-Pumping Water Function for Efficiency Solar Steam Generation, *ACS Appl. Mater. Interfaces*, 2020, **12**(23), 26033–26040.
- 164 G. Chen, J. Sun, Q. Peng, Q. Sun, G. Wang, Y. Cai, X. Gu, Z. Shuai and B. Z. Tang, Biradical-Featured Stable Organic-Small-Molecule Photothermal Materials for Highly Efficient Solar-Driven Water Evaporation, *Adv. Mater.*, 2020, **32**(29), 1908537.
- 165 P. Zhang, Q. Liao, H. Yao, H. Cheng, Y. Huang, C. Yang, L. Jiang and L. Qu, Three-dimensional water evaporation on a macroporous vertically aligned graphene pillar array under one sun, *J. Mater. Chem. A*, 2018, **6**(31), 15303–15309.
- 166 L. Cui, P. Zhang, Y. Xiao, Y. Liang, H. Liang, Z. Cheng and L. Qu, High Rate Production of Clean Water Based on the Combined Photo-Electro-Thermal Effect of Graphene Architecture, *Adv. Mater.*, 2018, **30**(22), 1706805.
- 167 H. Liang, Q. Liao, N. Chen, Y. Liang, G. Lv, P. Zhang, B. Lu and L. Qu, Thermal Efficiency of Solar Steam Generation Approaching 100% through Capillary Water Transport, *Angew. Chem., Int. Ed.*, 2019, 19041–19046.
- 168 X. Lin, J. Chen, Z. Yuan, M. Yang, G. Chen, D. Yu, M. Zhang, W. Hong and X. Chen, Integrative solar absorbers for highly efficient solar steam generation, *J. Mater. Chem. A*, 2018, **6**(11), 4642–4648.
- 169 F. Gong, H. Li, W. Wang, J. Huang, D. Xia, J. Liao, M. Wu and D. V. Papavassiliou, Scalable, eco-friendly and ultrafast solar steam generators based on one-step melamine-derived carbon sponges toward water purification, *Nano Energy*, 2019, **58**, 322–330.
- 170 Q. Tian, F. Jiang, R. Zou, Q. Liu, Z. Chen, M. Zhu, S. Yang, J. Wang, J. Wang and J. Hu, Hydrophilic Cu₉S₅ Nanocrystals: A Photothermal Agent with a 25.7% Heat Conversion Efficiency for Photothermal Ablation of Cancer Cells in Vivo, *ACS Nano*, 2011, **5**(12), 9761–9771.
- 171 D. Huang, X. Yan, M. Yan, G. Zeng, C. Zhou, J. Wan, M. Cheng and W. Xue, Graphitic Carbon Nitride-Based Heterojunction Photoactive Nanocomposites: Applications and Mechanism Insight, *ACS Appl. Mater. Interfaces*, 2018, **10**(25), 21035–21055.
- 172 C. M. Hessel, V. P. Pattani, M. Rasch, M. G. Panthani, B. Koo, J. W. Tunnell and B. A. Korgel, Copper Selenide Nanocrystals for Photothermal Therapy, *Nano Lett.*, 2011, **11**(6), 2560–2566.

- 173 J. Li and N. Wu, Semiconductor-based photocatalysts and photoelectrochemical cells for solar fuel generation: a review, *Catal. Sci. Technol.*, 2015, **5**, 1360–1384.
- 174 M. Gao, L. Zhu, C. K. Peh and G. W. Ho, Solar absorber material and system designs for photothermal water vaporization towards clean water and energy production, *Energy Environ. Sci.*, 2019, **12**(3), 841–864.
- 175 X. Chen, L. Liu, P. Y. Yu and S. S. Mao, Increasing Solar Absorption for Photocatalysis with Black Hydrogenated Titanium Dioxide Nanocrystals, *Science*, 2011, **331**(6018), 746–750.
- 176 S. Yin, H. Yamaki, M. Komatsu, Q. Zhang, J. Wang, Q. Tang, F. Saito and T. Sato, Preparation of nitrogen-doped titania with high visible light induced photocatalytic activity by mechanochemical reaction of titania and hexamethylenetetramine, *J. Mater. Chem.*, 2003, **13**, 2996–3001.
- 177 J. Wang, Y. Li, L. Deng, N. Wei, Y. Weng, S. Dong, D. Qi, J. Qiu, X. Chen and T. Wu, High-Performance Photothermal Conversion of Narrow-Bandgap Ti_2O_3 Nanoparticles, *Adv. Mater.*, 2017, **29**(3), 1603730.
- 178 M. Ye, J. Jia, Z. Wu, C. Qian, R. Chen, P. G. O'Brien, W. Sun, Y. Dong and G. A. Ozin, Synthesis of Black TiO_xNanoparticles by Mg Reduction of TiO₂Nanocrystals and their Application for Solar Water Evaporation, *Adv. Energy Mater.*, 2017, **7**(4), 1601811.
- 179 G. Zhu, J. Xu, W. Zhao and F. Huang, Constructing Black Titania with Unique Nanocage Structure for Solar Desalination, *ACS Appl. Mater. Interfaces*, 2016, **8**(46), 31716–31721.
- 180 C. Song, D. Qi, Y. Han, Y. Xu, H. Xu, S. You, W. Wang, C. Wang, Y. Wei and J. Ma, Volatile-Organic-Compound-Intercepting Solar Distillation Enabled by a Photothermal/Photocatalytic Nanofibrous Membrane with Dual-Scale Pores, *Environ. Sci. Technol.*, 2020, **54**(14), 9025–9033.
- 181 G. Wang, B. Huang, X. Ma, Z. Wang, X. Qin, X. Zhang, Y. Dai and M. Whangbo, Cu₂(OH)PO₄, a Near-Infrared-Activated Photocatalyst, *Angew. Chem. Int. Ed.*, 2013, **52**(18), 4810–4813.
- 182 Z. Hua, B. Li, L. Li, X. Yin, K. Chen and W. Wang, Designing a Novel Photothermal Material of Hierarchical Microstructured Copper Phosphate for Solar Evaporation Enhancement, *J. Phys. Chem. C*, 2017, **121**(1), 60–69.
- 183 J. Liu, Y. Li, J. Ke, S. Wang, L. Wang and H. Xiao, Black NiO-TiO₂ nanorods for solar photocatalysis: Recognition of electronic structure and reaction mechanism, *Appl. Catal., B*, 2018, **224**, 705–714.
- 184 D. D. Qin, Y. J. Zhu, R. L. Yang and Z. C. Xiong, A salt-resistant Janus evaporator assembled from ultralong hydroxyapatite nanowires and nickel oxide for efficient and recyclable solar desalination, *Nanoscale*, 2020, **12**(12), 6717–6728.
- 185 M. Tsai, S. H. Su, J.-K. Chang, D.-S. Tsai, C. Chen, C.-I. Wu, L. Li, L. Chen and J. He, Monolayer MoS₂ heterojunction solar cells, *ACS Nano*, 2014, **8**(8), 8317–8322.
- 186 M. Bernardi, M. Palummo and J. Grossman, Extraordinary sunlight absorption and one nanometer thick photovoltaics using two-dimensional monolayer materials, *Nano Lett.*, 2013, **13**(8), 3664–3670.
- 187 D. Xu, Z.-D. Li, L. Li and J. Wang, Insights into the Photothermal Conversion of 2D MXene Nanomaterials: Synthesis, Mechanism, and Applications, *Adv. Funct. Mater.*, 2020, **30**, 2000712.
- 188 X. Wang, N. D. Mansukhani, L. M. Guiney, Z. Ji, C. H. Chang, M. Wang, Y.-P. Liao, T.-B. Song, B. Sun, R. Li, T. Xia, M. C. Hersam and A. E. Nel, Differences in the Toxicological Potential of 2D versus Aggregated Molybdenum Disulfide in the Lung, *Small*, 2015, **11**(38), 5079–5087.
- 189 Z. Zhou, B. Li, C. Shen, D. Wu, H. Fan, J. Zhao, H. Li, Z. Zeng, Z. Luo, L.-F. Ma and C. Tan, Metallic 1T Phase Enabling MoS₂ Nanodots as an Efficient Agent for Photoacoustic Imaging Guided Photothermal Therapy in the Near-Infrared-II Window, *Small*, 2020, 202004173.
- 190 K. Kasinathan, B. Murugesan, N. Pandian, S. Mahalingam, B. Selvaraj and K. Marimuthu, Synthesis of biogenic chitosan-functionalized 2D layered MoS₂ hybrid nanocomposite and its performance in pharmaceutical applications: In-vitro antibacterial and anticancer activity, *Int. J. Biol. Macromol.*, 2020, **149**, 1019–1033.
- 191 C. Cai, Z. Wei, Y. Huang and Y. Fu, Wood-inspired superelastic MXene aerogels with superior photothermal conversion and durable superhydrophobicity for clean-up of super-viscous crude oil, *Chem. Eng. J.*, 2020, 127772.
- 192 M. Yu, P. Xu, J. Yang, L. Ji and C. Li, Self-Growth of MoS₂ Sponge for Highly Efficient Photothermal Cleanup of High-Viscosity Crude Oil Spills, *Adv. Mater. Interfaces*, 2020, **7**, 1901671.
- 193 D. Ghim, Q. Jiang, S. Cao, S. Singamaneni and Y.-S. Jun, Mechanically interlocked 1T/2H phases of MoS₂ nanosheets for solar thermal water purification, *Nano Energy*, 2018, **53**, 949–957.
- 194 Q. Wang, Q. Guo, F. Jia, Y. Li and S. Song, Facile Preparation of Three-Dimensional MoS₂ Aerogels for Highly Efficient Solar Desalination, *ACS Appl. Mater. Interfaces*, 2020, **12**(29), 32673–32680.
- 195 R. Chen, X. Wang, Q. Gan, T. Zhang, K. Zhu and M. Ye, A bifunctional MoS₂-based solar evaporator for both efficient water evaporation and clean freshwater collection, *J. Mater. Chem. A*, 2019, **7**(18), 11177–11185.
- 196 Q. Wang, F. Jia, A. Huang, Y. Qin, S. Song, Y. Li and M. A. C. Arroyo, MoS₂@sponge with double layer structure for high-efficiency solar desalination, *Desalination*, 2020, **481**, 114359.
- 197 Z. Guo, G. Wang, X. Ming, T. Mei, J. Wang, J. Li, J. Qian and X. Wang, PEGylated Self-Growth MoS₂ on a Cotton Cloth Substrate for High-Efficiency Solar Energy Utilization, *ACS Appl. Mater. Interfaces*, 2018, **10**(29), 24583–24589.
- 198 W. Wang, J. Jiang, T. Ding, C. Wang, J. Zuo and Q. Yang, Alternative Synthesis of CuFeSe₂ Nanocrystals with Magnetic and Photoelectric Properties, *ACS Appl. Mater. Interfaces*, 2015, **7**(4), 2235–2241.
- 199 S. Ghosh, T. Avellini, A. Petrelli, I. Kriegel, R. Gaspari, G. Almeida, G. Bertoni, A. Cavalli, F. Scotognella, T. Pellegrino and L. Manna, Colloidal CuFeS₂ Nanocrystals: Intermediate

- Fe d-Band Leads to High Photothermal Conversion Efficiency, *Chem. Mater.*, 2016, **28**, 4848–4858.
- 200 H. Liu, C. Chen, H. Wen, R. Guo, N. A. Williams, B. Wang, F. Chen and L. Hu, Narrow bandgap semiconductor decorated wood membrane for high-efficiency solar-assisted water purification, *J. Mater. Chem. A*, 2018, **6**(39), 18839–18846.
- 201 J. P. Perdew, K. Burke and M. Ernzerhof, Generalized Gradient Approximation Made Simple, *Phys. Rev. Lett.*, 1996, **77**(18), 3865–3868.
- 202 Y. Ding, B. Xiao, G. Tang and J. Hong, Transport Properties and High Thermopower of SnSe₂:A Full Ab-Initio Investigation, *J. Phys. Chem. C*, 2017, **121**(1), 236.
- 203 Z. Tahir, S. Kim, F. Ullah, S. Lee, J. H. Lee, N. W. Park, M. J. Seong, S. K. Lee, T. S. Ju, S. Park, J. S. Bae, J. I. Jang and Y. S. Kim, Highly Efficient Solar Steam Generation by Glassy Carbon Foam Coated with Two-Dimensional Metal Chalcogenides, *ACS Appl. Mater. Interfaces*, 2020, **12**(2), 2490–2496.
- 204 M. Huang, M. Wang, C. Chen, Z. Ma, X. Li, J. Han and Y. Wu, Broadband Black-Phosphorus Photodetectors with High Responsivity, *Adv. Mater.*, 2016, **28**(18), 3481–3485.
- 205 C. Yang, D. Xu, W. Peng, Y. Li, G. Zhang, F. Zhang and X. Fan, Ti₂C₃T_x nanosheets as photothermal agents for near-infrared responsive hydrogels, *Nanoscale*, 2018, **10**(32), 15387–15392.
- 206 B. Klemmed, L. Besteiro, A. Benad, M. Georgi, Z. Wang, A. Govorov and A. Eychmüller, Hybrid Plasmonif Aerogel Materials as Optical Superheaters with Engineered Resonances, *Angew. Chem., Int. Ed.*, 2019, **59**, 1696–1702.
- 207 W. Cai, X. Mu, Y. Pan, Z. Li, J. Wang, X. Zhou, W. Guo, W. Hu, L. Song and Y. Hu, Black Phosphorous Nanosheets: A Novel Solar Vapor Generator, *Sol. RRL*, 2020, **4**(4), 1900537.
- 208 M. Serrano-Ruiz, M. Caporali, A. Ienco, V. Piazza, S. Heun and M. Peruzzini, The Role of Water in the Preparation and Stabilization of High-Quality Phosphorene Flakes, *Adv. Mater. Interfaces*, 2016, **3**(3), 1500441.
- 209 M. Li, Q. Zhao, S. Zhang, D. Li, H. Li, X. Zhang and B. Xing, Facile passivation of black phosphorus nanosheets via silica coating for stable and efficient solar desalination, *Environ. Sci.: Nano*, 2020, **7**(2), 414–423.
- 210 Q. Ma, P. Yin, M. Zhao, Z. Luo, Y. Huang, Q. He, Y. Yu, Z. Liu, Z. Hu, B. Chen and H. Zhang, MOF-Based Hierarchical Structures for Solar-Thermal Clean Water Production, *Adv. Mater.*, 2019, **31**(17), 201808249.
- 211 Y. Guo, H. Lu, F. Zhao, X. Zhou, W. Shi and G. Yu, Biomass-Derived Hybrid Hydrogel Evaporators for Cost-Effective Solar Water Purification, *Adv. Mater.*, 2020, **32**(11), 201907061.
- 212 Y. Xu, J. Ma, Y. Han, J. Zhang, F. Cui, Y. Zhao, X. Li and W. Wang, Multifunctional CuO Nanowire Mesh for Highly Efficient Solar Evaporation and Water Purification, *ACS Sustainable Chem. Eng.*, 2019, **7**(5), 5476–5485.
- 213 L. Zhang, L. Mu, Q. Zhou and X. Hu, Solar-assisted fabrication of dimpled 2H-MoS₂ membrane for highly efficient water desalination, *Water Res.*, 2020, **170**, 115367.
- 214 Y. Zhou, Q. Lu, Q. Liu, H. Yang, J. Liu, J. Zhuang, W. Shi and X. Wang, Architecting Hybrid Donor-Acceptor Dendritic Nanosheets Based on Polyoxometalate and Porphyrin for High-Yield Solar Water Purification, *Adv. Funct. Mater.*, 2022, **32**, 2112159.
- 215 S. Ma, K. Chen, Y. Qiu, L. Gong, G.-M. Pan, Y.-j. Lin, Z. Hao, L. Zhou and Q. Wang, Controlled growth of CdS CuT xS lateral heteroshells on Au nanoparticles with improved photocatalytic activity and photothermal efficiency, *J. Mater. Chem.*, 2019, **7**, 3408–3414.
- 216 Y. Chang, Y. Cheng, Y. Feng, H. Jian, L. Wang, X. Ma, X. Li and H. Zhang, Resonance Energy Transfer-Promoted Photothermal and Photodynamic Performance of Gold-Copper Sulfide Yolk-Shell Nanoparticles for Chemophototherapy of Cancer, *Nano Lett.*, 2018, **18**(2), 886–897.
- 217 Y. Liu, Z. Zhang, Y. Fang, B. Liu, J. Huang, F. Miao, Y. Bao and B. Dong, IR-Driven strong plasmonic-coupling on Ag nanorices/W18O49 nanowires heterostructures for photo/thermal synergistic enhancement of H₂ evolution from ammonia borane, *Appl. Catal., B*, 2019, **252**, 164–173.
- 218 P. Sun, W. Wang, W. Zhang, S. Zhang, J. Gu, L. Yang, D. Pantelić, B. Jelenković and D. Zhang, 3D Interconnected Gyroid Au–CuS Materials for Efficient Solar Steam Generation, *ACS Appl. Mater. Interfaces*, 2020, **12**(31), 34837–34847.
- 219 Y. Yang, X. Yang, L. Fu, M. Zou, A. Cao, Y. Du, Q. Yuan and C.-H. Yan, Two-Dimensional Flexible Bilayer Janus Membrane for Advanced Photothermal Water Desalination, *ACS Energy Lett.*, 2018, **3**(5), 1165–1171.
- 220 R. Cui, J. Wei, C. Du, S. Sun, C. Zhou, H. Xue and S. Yang, Engineering trace AuNPs on monodispersed carbonized organosilica microspheres drives highly efficient and low-cost solar water purification, *J. Mater. Chem. A*, 2020, **8**(26), 13311–13319.
- 221 X. Meng, J. Yang, S. Ramakrishna, Y. Sun and Y. Dai, Gradient-aligned Au/graphene meshes with confined heat at multiple levels for solar evaporation and anti-gravity catalytic conversion, *J. Mater. Chem. A*, 2020, **8**(32), 16570–16581.
- 222 J. Xu, F. Xu, M. Qian, Z. Li, P. Sun, Z. Hong and F. Huang, Copper nanodot-embedded graphene urchins of nearly full-spectrum solar absorption and extraordinary solar desalination, *Nano Energy*, 2018, **53**, 425–431.
- 223 F. S. Awad, H. D. Kiriarachchi, K. M. AbouZeid, Ü. Özgür and M. S. El-Shall, Plasmonic Graphene Polyurethane Nanocomposites for Efficient Solar Water Desalination, *ACS Appl. Energy Mater.*, 2018, **1**(3), 976–985.
- 224 J. Huang, Y. He, M. Chen, B. Jiang and Y. Huang, Solar evaporation enhancement by a compound film based on Au@TiO₂ core-shell nanoparticles, *Sol. Energy*, 2017, **155**, 1225–1232.
- 225 H. Li, Y. He, Z. Liu, B. Jiang and Y. Huang, A flexible thin-film membrane with broadband Ag@TiO₂ nanoparticle for high-efficiency solar evaporation enhancement, *Energy*, 2017, **139**, 210–219.
- 226 M. Gao, P. K. N. Connor and G. W. Ho, Plasmonic photothermic directed broadband sunlight harnessing for

- seawater catalysis and desalination, *Energy Environ. Sci.*, 2016, **9**, 3151–3160.
- 227 L. Yi, S. Ci, S.-L. Luo, P. Shao, Y. Hou and Z. Wen, Scalable and low-cost synthesis of black amorphous Al-Ti-O nanostructure for high-efficient photothermal desalination, *Nano Energy*, 2017, **41**, 600–608.
- 228 Y. Xu, J. Ma, Y. Han, H. Xu, Y. Wang, D. Qi and W. Wang, A simple and universal strategy to deposit Ag/polypyrrole on various substrates for enhanced interfacial solar evaporation and antibacterial activity, *Chem. Eng. J.*, 2020, **384**, 123379.
- 229 M. Lin, C. Guo, J. Li, D. Zhou, K. Liu, X. Zhang, T. Xu, H. Zhang, L. Wang and B. Yang, Polypyrrole-Coated Chainlike Gold Nanoparticle Architectures with the 808 nm Photothermal Transduction Efficiency up to 70%, *ACS Appl. Mater. Interfaces*, 2014, **6**(8), 5860–5868.
- 230 S. Chen, Z. Sun, W. Xiang, C. Shen, Z. Wang, X. Jia, J. Sun and C.-J. Liu, Plasmonic wooden flower for highly efficient solar vapor generation, *Nano Energy*, 2020, **76**, 104998.
- 231 A. Sun, X. Hou and X. Hu, Super-performance photothermal conversion of 3D macrostructure graphene-CuFeSe₂ aerogel contributes to durable and fast clean-up of highly viscous crude oil in seawater, *Nano Energy*, 2020, **70**, 104511.
- 232 X. Chang, Y. Zhang, X. Weng, P. Su, W. Wu and Y. Mo, Red-Shifting versus Blue-Shifting Hydrogen Bonds: Perspective from Ab Initio Valence Bond Theory, *J. Phys. Chem. A*, 2016, **120**(17), 2749–2756.
- 233 L. Guo, J. Gong, C. Song, Y. Zhao, B. Tan, Q. Zhao and S. Jin, Donor-Acceptor Charge Migration System of Superhydrophilic Covalent Triazine Framework and Carbon Nanotube toward High Performance Solar Thermal Conversion, *ACS Energy Lett.*, 2020, **5**(4), 1300–1306.